International Journal of Solids and Structures 50 (2013) 1879–1896

Contents lists available at SciVerse ScienceDirect

International Journal of Solids and Structures

journal homepage: www.elsevier.com/locate/ijsolstr

Microstructure-performance relations of ultra-high-performance concrete accounting for effect of alpha-quartz-to-coesite silica phase transformation

Jonathan J. Buck, David L. McDowell, Min Zhou *

The George W. Woodruff School of Mechanical Engineering, Georgia Institute of Technology, Atlanta, GA 30332-0405, USA
The School of Materials Science and Engineering, Georgia Institute of Technology, Atlanta, GA 30332-0405, USA

ARTICLE INFO

Article history:
Received 11 May 2012
Received in revised form 27 January 2013
Available online 21 February 2013

Keywords:
Ultra-high-performance concrete
Dynamic loading
Phase transformation
Microstructure
Energy dissipation
Load-carrying capacity

ABSTRACT

The effect of the α-quartz-to-coesite silica phase transformation on the load-carrying and energy-dissipation capacities of ultra-high-performance concrete (UHPC) under dynamic loading with hydrostatic pressures of up to 10 GPa is evaluated. The model resolves essential deformation and failure mechanisms and provides a phenomenological account of the transformation. Four modes of energy dissipated are tracked, including inelastic deformation, distributed cracking, interfacial friction, and the energy dissipated through transformation of the quartz aggregate. Simulations are carried out over a range of volume fractions of the constituent phases. Results show that the phase transformation has a significant effect on the energy-dissipation capacity of UHPC for the conditions studied. Although transformation accounts for less than 2% of the total energy dissipation, the transformation leads to a twofold increase in the crack density and yields almost an 18% increase in the overall energy dissipation. Structure-response relations that can be used for materials design are established.

1. Introduction

Ultra high-performance concrete (UHPC) is often used in structures that are intended to provide protection against a variety of threat scenarios, including blast and impact (Cavil et al., 2006). These intense loading regimes lead to elevated temperatures and pressures. Under such conditions, the material constituents can change phase, which can drastically alter the dynamic response of the material. Understanding the mechanical behavior alone, however, is not enough to characterize a material in these loading regimes. Dynamic loading of UHPC is inherently a coupled multiphysics process involving mechanical, thermal, and phase transformation behavior.

The mechanical aspects, including fracture, friction, and bulk granular flow, lead to internal temperature rises within a UHPC structure and hydrostatic pressures on the order of multiple GPa. These internal temperature rises and large pressures within UHPC can induce phase transformations in the constituents (Wang et al., 2010). One such transformation is the solid-state transformation of quartz from the α-quartz phase to the coesite phase. It should be noted that this transformation has not been fully quantified experimentally and further investigation is still needed. Increased temperature can also lead to thermal softening of the constituents. Phase transformations can lead to stiffness and density changes, as well as additional fracture that can lead to further dissipation and temperature increases, which in turn alter the mechanical behavior. This interaction between mechanical, thermal, and phase transformational processes during dynamic loading of UHPC ultimately determines its load-carrying and energy-dissipation capacities. Properly accounting for the coupling between these processes in the regime of dynamic loading environments can provide for a more complete assessment of the load-carrying and energy-dissipation capacities. Because UHPC is a complex heterogeneous material, which, like ordinary forms of concrete, contains large amounts of quartz sand (Rong et al., 2010), it is of interest to account for these behaviors to better understand and take advantage of such mechanisms. For example, to most effectively tailor the energy-dissipation capacity of UHPC structures and enhance their survivability under extreme loading environments (e.g., blast and impact), the fundamental processes that give rise to energy dissipation must be understood.

Numerical simulations at the microstructural scale offer an attractive means of accounting for the many coupled processes that occur during a loading process because of the complexity involved with tracking of all the mechanisms simultaneously. There have been simulations that do account for temperature- and pressure-dependent properties in concrete, but the focus of such work has been on either thermal and mass transport properties (Flynn, 1998), or on the static mechanical behavior (Morsy et al.,

* Corresponding author at: The George W. Woodruff School of Mechanical Engineering, Georgia Institute of Technology, Atlanta, GA 30332-0405, USA. Tel.: +1 404 894 3294.
E-mail address: min.zhou@gatech.edu (M. Zhou).

0020-7683/$ - see front matter © 2013 Elsevier Ltd. All rights reserved.
http://dx.doi.org/10.1016/j.ijsolstr.2013.01.042

2010; Omer, 2007; Naus, 2010; Handoo et al., 2002). More recent work has attempted to bridge the gap between mass transport properties and mechanical properties by simulating the damage initiation in UHPC exposed to rapid heating (Lammi et al., 2011). Numerical simulations of dynamic loading of UHPC at the microstructural scale have been performed that included an explicit account of the quartz aggregate, along with various other phases, including porosity, steel fibers, and the cementitious matrix (Aragao et al., 2010; Lammi et al., 2011; Ellis et al., 2012).

The authors are presently unaware of any work reported in the literature that accounts for phase change within UHPC at the mesostructural level with the ultimate goal of characterizing the mechanical behavior of the material under high strain-rate dynamic loading. Analysis techniques capable of capturing the coupled nature of the material response are needed to inform the design of UHPC structures that must to be resilient to extreme loading environments. Before UHPC structures can be tailored to specific applications, the behavior of each constituent during energetic blast and impact events, which induce very high strain-rate deformation, must be well characterized.

In a companion work (Buck et al., 2012), a parametric study was performed to assess the effects of microstructure phase volume fractions on the dynamic mechanical behavior of UHPC without thermal or phase transformational considerations. Results showed that the volume fractions of the constituents have more influence on the energy dissipation than the load-carrying capacity, inelastic deformation is the source of over 70% of the energy dissipation, and the presence of porosity changes the role of fibers in the dissipation process. The goal of the present study is to address both the mechanical and transformational aspects of the deformation process. In particular, one aim of this paper is to quantify the effect of the α-quartz-to-coesite phase transformation in UHPC subject to energetic impact events. This will be accomplished by comparing the load-carrying and energy-dissipation capacities in UHPC with and without the inclusion of a phenomenological model capable of phenomenologically capturing the effects of the aforementioned phase transformation. As part of the analysis, the development and validation of the phenomenological model are discussed. Finally, updated microstructure performance-relation maps are developed to account for the effect of phase transformation of quartz on the response of the UHPC analyzed. The same micromechanical cohesive finite element model (CFEM) used in the first part of this study (Buck et al., 2012) is adopted to allow explicit resolution of the constituents in the concrete microstructure, including the cementitious matrix, aggregate, fibers, and voids. The model also allows explicit account of crack formation and frictional interaction between crack surfaces that come into contact under compression. The volume fractions of phases of the microstructure are systematically varied to delineate the effects of each material constituent. This approach enables the contributions of different dissipation mechanisms (bulk inelasticity, fracture/crack formation, and interfacial friction) to be tracked and quantified. The simulations are carried out at strain rates on the order of $10^5\ s^{-1}$ and pressures between 1 and 10 GPa.

2. Cohesive finite element model

A cohesive finite element model framework is used in this paper to conduct the numerical simulations. The framework is capable of resolving four distinct constituent phases, including the cementitious matrix, quartz aggregate, steel fibers, and voids. The framework also allows for the definition of interface properties so that fracture of interfaces and friction along crack faces can be considered. The 2D microstructures are 5 mm in width and 20 mm in height, as shown in Fig. 1. The framework makes use of a 2D plane strain assumption. The width or smaller dimension of this sample

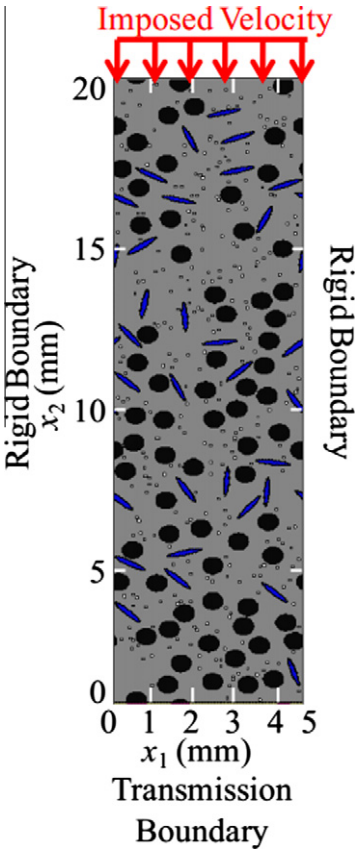

Fig. 1. Cohesive finite element model for UHPC microstructures with four constituent phases of UHPC, imposed velocity, periodic boundary conditions, cohesive elements, and infinite elements.

is nearly 10 times the size of the largest constituent (the quartz aggregate with a diameter of 600 μm) and is also large enough such that even constituents present at the lowest volume fraction (2.5%) appear approximately 15 times in the cementitious material. This is important with respect to the random instantiation of the microstructures. Too few appearances of the constituents could bias the results if the random generation process concentrated constituents in a particular region of the control area.

A velocity of 1000 m/s in the downward direction is imposed on the upper surface of the microstructures. Rigid boundary conditions on the sides of the microstructures allow the computations to approximate the overall conditions of uniaxial strain with significant confining stresses. A transmission boundary on the lower surface is used to allow for transmission of the stress wave without reflection. However, only data prior to the stress wave reaching the lower surface (first 6.0 μs) are considered, so the existence of the lower boundary does not affect the discussions here. It should be emphasized that the purpose of this study is to quantify the load-carrying and energy-dissipation capacities of UHPC as functions of the volume fractions of phases, rather than phase size or size distribution. The effect of morphology of the constituents is beyond the scope of the current work and is reserved for future study. Additional details are provided in the first part of this work (Buck et al., 2012).

3. Constitutive relations

3.1. Cementitious matrix

Cementitious materials are both pressure-sensitive and rate-sensitive, so the constitutive relation used must be able to capture

both aspects of the behavior. In this study, the Drucker–Prager model is used for the cementitious matrix (Drucker and Prager, 1952).The Drucker–Prager relation assumes the yield condition

$$F = t - p\tan(\beta) - d \leqslant 0, \tag{1}$$

where

$$t = \frac{1}{2}q\left[1 + \frac{1}{K} - \left(1 - \frac{1}{K}\right)\left(\frac{r}{q}\right)^3\right]. \tag{2}$$

In the above equations, p is the hydrostatic pressure, β is the internal friction angle in the meridional stress plane, d is the yield stress of the material under pure shear, q is the von Mises equivalent stress, given by $q = \sqrt{\frac{3}{2}\mathbf{S} : \mathbf{S}}$, K is the ratio between the yield stress in triaxial tension and the yield stress in triaxial compression, and r is the third invariant of the deviatoric stress, given by $r = \sqrt[3]{\frac{9}{2}\mathbf{S}\cdot\mathbf{S} : \mathbf{S}}$. In the preceding expressions, $\mathbf{S}$ is the deviatoric stress tensor. Parameter K allows for tension–compression asymmetry on any arbitrary π-plane. To ensure a convex yield surface, the value of K is restricted to the range $0.778 \leqslant K \leqslant 1.0$. Setting $K = 1$ removes the dependence on the third invariant of the deviatoric stress, and Eq. (1) reduces to the classical Drucker–Prager yield criterion (Drucker and Prager, 1952). Furthermore, when $K = 1$ and $\beta = 0$, Eq. (1) reduces to the von Mises yield criterion. The Drucker–Prager yield criterion is shown schematically in Fig. 2. Fig. 2(a) shows the shear stress as a function of hydrostatic pressure. The slope is governed by the parameter β, and the vertical axis intercept is determined by the yield stress under pure shear. Fig. 2(b) shows the yield function in the π-plane for $K = 0.8$ (the value used in this study) as well as $K = 1$ for comparison (Abaqus v6.10 Theory Manual, 2010).

Because cementitious paste exhibits dilatation and is a non-associative material, the yield function F does not serve as the plastic flow potential. Instead, a scalar flow potential G is chosen such that

$$G = t - p\tan(\psi), \tag{3}$$

where ψ is the dilation angle. After yielding, a material with non-associated flow has the rate of plastic deformation tensor

$$\mathbf{D}^{pl} = \frac{\dot{\bar{\varepsilon}}^{pl}}{c}\frac{\partial G}{\partial \boldsymbol{\sigma}}, \tag{4}$$

where $\dot{\bar{\varepsilon}}^{pl}$ is the equivalent plastic strain rate, defined by

$$\dot{\bar{\varepsilon}}^{pl} = \sqrt{\frac{2}{3}\mathbf{D}^{pl} : \mathbf{D}^{pl}} \tag{5}$$

and

$$c = 1 - \frac{1}{3}\tan\psi. \tag{6}$$

The values used for the parameters in the Drucker–Prager constitutive relation are provided in Table 1 (Swamy and Mangat, 1974).

Table 1
Parameters used in the Drucker–Prager constitutive relation.

Density (g/cm^3)	2.4
Elastic modulus (GPa)	22.9
Poisson's ratio	0.2
Quasi-static compressive strength (MPa)	40
Friction angle β (degrees)	28
Dilation angle ψ (degrees)	20
K	0.8

3.2. Quartz aggregate

At ambient conditions, quartz exists as α-quartz, which exhibits a trigonal crystal structure (Swamy and Mangat, 1974). Above a pressure of 2.35 GPa and at ambient temperature, quartz undergoes a solid-state phase transformation to coesite, which exhibits a monoclinic crystal structure. This transformation is accompanied by an 8.82% decrease in volume (Zhou, 2005) and a 0.45% decrease in internal energy (Boettger and Lyon, 1990). Coesite has an enthalpy of formation of −907.25 kJ/mol (Bose and Ganguly, 1995). This study will only consider the change in volume, and the process is assumed to be isothermal. It should be noted that α-quartz also undergoes a pressure- and temperature-dependent transformation to β-quartz at temperatures above approximately 600 °C (Wang et al., 2010). This phase transformation is accompanied by a volume increase, as well as the dehydration of the hydrated cementitious products. At even higher temperatures, dehydroxylation of the cementitious products occurs. Here, only the transformation to coesite and the associated volume change are considered. This focus allows the effects of this transformation on material behavior to be analyzed. With sufficient input data, the approach can be extended to study the effects of other phase changes in the future.

Due to the limited symmetry of trigonal and monoclinic crystals, the crystalline natures of α-quartz and coesite dictate that they are anisotropic. However, for simplicity, quartz is modeled as an isotropic material through the use of effective isotropic properties obtained using the Voigt–Reuss–Hill averaging technique (Hill, 1952). This procedure is implemented over a range of pressures so that the material properties used in the simulations reflect relevant pressure-dependence, as shown in Fig. 3.

The first step is the collection of elastic constants for α-quartz and coesite as a function of pressure. Trigonal crystal structures have six independent elastic constants. Since the data available in the literature (Calderon et al., 2007) only extend up to 1.0 GPa, it is necessary to extrapolate the elastic constants of α-quartz up to the transition pressure of 2.35 GPa using a linear curve fit. The monoclinic structure of coesite possesses fewer symmetries and requires 13 elastic constants (Kimizuka et al., 2008).

Next, four sets of values are chosen for the purposes of deriving effective isotropic properties: (1) α-quartz constants at 0.0 GPa, (2)

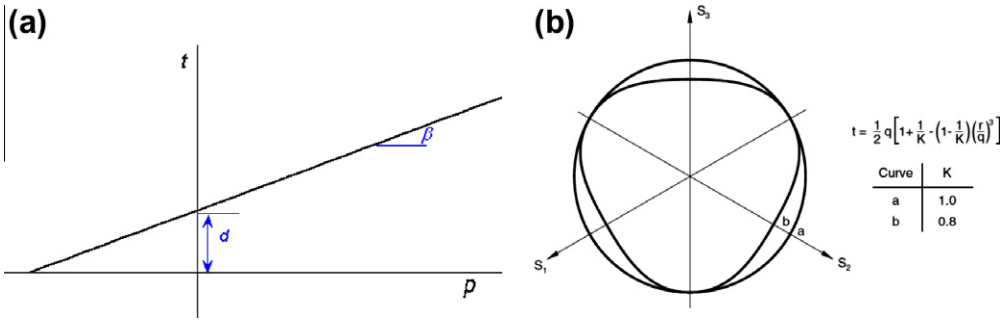

Fig. 2. Drucker–Prager yield criterion (a) in t–p plane, and (b) in the π-plane Abaqus v6.10 Theory Manual, 2010.

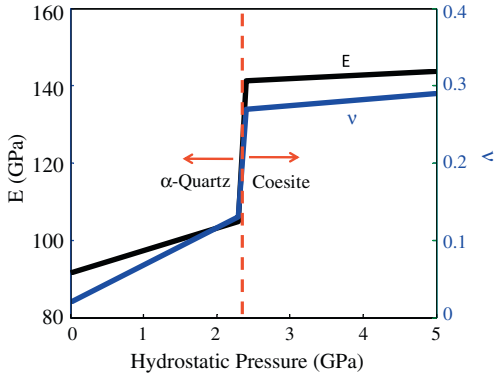

Fig. 3. Effective isotropic elastic properties for α-quartz and coesite as functions of hydrostatic pressure.

α-quartz constants at 2.35 GPa, (3) coesite constants at 2.35 GPa, and (4) coesite constants at 10.0 GPa. The Voigt–Reuss–Hill averaging technique (Hill, 1952) is used at each pressure level to calculate four sets of isotropic properties. Elastic constants pertaining to pressures between points 1 and 2 and between points 3 and 4 in Fig. 3 can be found through interpolation.

The first step of the Voigt–Reuss–Hill averaging technique is to calculate the Voigt effective stiffness. The Voigt stiffness assumes uniform strain and provides an upper bound to elastic moduli. The Voigt effective bulk modulus K_V is defined by

$$9K_V = (c_{11} + c_{22} + c_{33}) + 2(c_{12} + c_{23} + c_{31}), \tag{7}$$

where c_{ij} are the components of the elastic stiffness tensor. The Voigt shear modulus G_V is defined as

$$15G_V = (c_{11} + c_{22} + c_{33}) - (c_{12} + c_{23} + c_{31}) + 3(c_{44} + c_{55} + c_{66}), \tag{8}$$

where c_{ij} are the components of the elastic stiffness tensor.

Similarly, the Reuss effective stiffness assumes constant stress and provides a lower bound to the elastic moduli. The Reuss effective bulk modulus K_R is defined as

$$1/K_R = (s_{11} + s_{22} + s_{33}) + 2(s_{12} + s_{23} + s_{31}), \tag{9}$$

where s_{ij} are the components of the elastic compliance tensor. The Reuss shear modulus G_R is defined as

$$15/G_R = 4(s_{11} + s_{22} + s_{33}) - 4(s_{12} + s_{23} + s_{31}) + 3(s_{44} + s_{55} + s_{66}), \tag{10}$$

where s_{ij} are the components of the elastic compliance tensor.

Finally, the Voigt–Reuss–Hill effective bulk modulus is simply the arithmetic mean of the Voigt stiffness and the Reuss stiffness, i.e.,

$$K_{VRH} = \frac{K_R + K_V}{2}. \tag{11}$$

Similarly, the Voigt–Reuss–Hill effective shear modulus is given by

$$G_{VRH} = \frac{G_R + G_V}{2}. \tag{12}$$

Since $K_R \leqslant K \leqslant K_V$ and $G_R \leqslant G \leqslant G_V$, where K and G are the true values of the stiffness and shear modulus, respectively, the Voigt–Reuss–Hill average provides a satisfactory estimate of the elastic properties if the quartz grains are assumed to be isotropic. At the grain level, the quartz aggregate is, of course, anisotropic. However, at the mesostructural level of UHPC, where the interest is more in the collective response of the entire structure and not the behavior of any individual grain, isotropy of the quartz aggregate is a reasonable assumption.

The Voigt, Reuss, and Voigt–Reuss–Hill stiffness values are summarized in Table 2. For clarity, the red line demarcates the boundary between α-quartz and coesite. In the last two columns of Table 2, the elastic modulus E and Poisson's ratio ν are calculated using the Voigt–Reuss–Hill bulk modulus and shear modulus according to standard elasticity relationships. The effective isotropic elastic properties are shown in Fig. 3. As in Table 2, the division between α-quartz and coesite is indicated by a red line. The values in between the numbers calculated in Table 2 represent simple linear interpolation.

The transformation of α-quartz into coesite is accompanied by a volume reduction of 8.82% (Zhou, 2005). The literature is not clear as to whether this volume reduction is with respect to the original, undeformed volume or with respect to the elastically deformed configuration just prior to transformation. For the purposes of this study, it is assumed that the 8.82% volume reduction is relative to the volume just prior to the transformation. Since the volume change (and deformation overall) in the aggregate prior to the phase transformation is on the order of 3% in the calculations of this paper, this assumption does not have a significant impact on the result. Specifically, if the original volume of a material element is V_0, assuming the transformation volume change to be relative to the original volume and assuming it to be relative to the deformed volume correspond to reckoning the transformation relative to V_0 and $0.97V_0$, respectively. To model this contraction, a methodology based on finite deformation kinematics has been developed. Assuming a multiplicative decomposition of the deformation gradient, the deformation of a quartz element can be shown schematically in Fig. 4. Here, R_0 represents the reference region, c_0 represents the initial center of the quartz element, and $\mathbf{x}$ represents the initial position. $\mathbf{F}^{el}$ is the deformation gradient associated the elastic deformation of the quartz. This leads to an intermediate state where R is the intermediate reference region, c is the center of the quartz element in the intermediate state, and $\mathbf{y}$ is the position. $\mathbf{F}^{tr}$ represents the deformation due to the phase transformation alone and leads to the final state where R^* is the reference region, c^* is the center, and y^* is the position. The final state can be reached through the combined deformation gradient $\mathbf{F} = \mathbf{F}^{tr} \cdot \mathbf{F}^{el}$. No other forms of inelastic deformation are considered. Natural quartz crystals do not display appreciable plastic deformation except under the combination of pressures and temperatures in excess of 1.5 GPa and 400 °C, respectively (Blacic and Christie, 1984). Furthermore, these data are for quasi-static strain rates. Although pressures in this study are in this regime, temperatures are not; internal temperature increases are not considered. Consequently, the failure mode of quartz is likely to be brittle fracture under the high-rate loading of this study.

The volumetric contraction can be described as proportional and isotropic scaling of the coordinates about the center of an element relative in the intermediate state in the form of

$$\mathbf{y}^* = \alpha(\mathbf{y} - \mathbf{c}) + \mathbf{c}. \tag{13}$$

In Eq. (13), α represents the amount of scaling in any direction corresponding to the desired volume change. Note that $\alpha < 1$ since the volume decreases upon transformation.

The deformation gradient due to the transformation alone is

$$\mathbf{F}^{tr} = \frac{\partial y^*}{\partial y} = \begin{bmatrix} \alpha & 0 & 0 \\ 0 & \alpha & 0 \\ 0 & 0 & \alpha \end{bmatrix} = \alpha \mathbf{I}. \tag{14}$$

Table 2
Voigt–Reuss–Hill average stiffness values for α-quartz and coesite at key pressure values.

Pressure (GPa)	*KV* (GPa)	*KR* (GPa)	*KVRH* (GPa)	*GV* (GPa)	*GR* (GPa)	*GVRH* (GPa)	*E* (GPa)	*ν*
0.0 (1 atm)	38.11	37.65	37.88	48.07	41.38	44.73	96.29	0.08
2.35	47.37	46.74	47.06	49.55	43.48	46.52	104.96	0.13
2.35	106.37	100.22	103.29	59.47	51.52	55.49	141.19	0.27
10.00	133.21	127.97	130.59	60.97	50.40	55.68	146.26	0.31

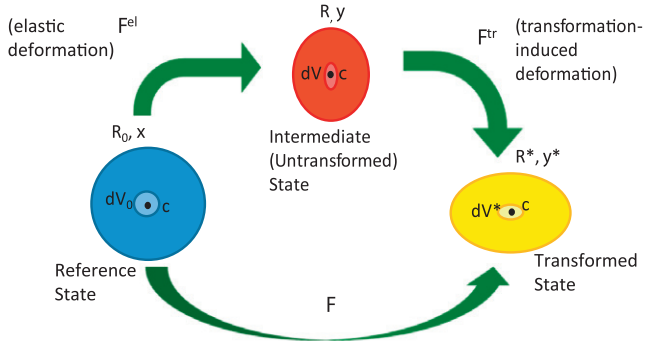

Fig. 4. Multiplicative decomposition of deformation gradient for accounting for the volume change associated with quartz phase change.

To determine α, note that

$$\frac{dV^*}{dV} = \det \mathbf{F}^{tr} = \alpha^3 = 0.9118. \tag{15}$$

Therefore, $\alpha = 0.9697$.

The total deformation gradient is

$$\mathbf{F} = (\alpha \mathbf{I}) \cdot \mathbf{F}^{el} = \alpha \mathbf{F}^{el}. \tag{16}$$

The logarithmic strain with respect to the intermediate state is then

$$\boldsymbol{\varepsilon}^{L^*} = \ln(\mathbf{V}^*) = \ln(\alpha \mathbf{V}) = \mathbf{I} \ln(\alpha) + \ln(\mathbf{V}) = \mathbf{I} \ln(\alpha) + \boldsymbol{\varepsilon}^{L}, \tag{17}$$

where **V** is the left stretch tensor. Finally, the Cauchy stress σ, or the true stress in the final state, is calculated in incremental form according to

$$d\boldsymbol{\sigma} = \mathbf{C} : d\boldsymbol{\varepsilon}^{L^*}, \tag{18}$$

where **C** is the fourth-order elastic stiffness tensor for quartz. To calculate the Cauchy stress at the $i+1$th time step, the Cauchy stress increment is simply added to the previous Cauchy stress, i.e.,

$$\boldsymbol{\sigma}^{i+1} = \boldsymbol{\sigma}^{i} + d\boldsymbol{\sigma}. \tag{19}$$

The above constitutive relations are implemented in the Abaqus/Explicit user material subroutine VUMAT (Abaqus v6.10 Theory Manual, 2010). To verify the proper implementation of the constitutive relations, the behavior of a block of α-quartz under uniform hydrostatic pressure is analyzed. Equal pressure loads are applied to five of the six faces of the cube, with the rear face fixed in the *Z* direction, creating a hydrostatic compression state of stress in the material. The load increases gradually from 0 to 9 GPa so that the behavior of the cube can be clearly observed both before and after the transition pressure of 2.35 GPa.

The behavior of the unit cube can be seen in Fig. 5(a), which shows the hydrostatic pressure as a function of uniaxial strain. Due to the symmetry of the model, all strain components are equal, as the strain represents the strain in any direction. A key observation from the figure is that, when the transition pressure of 2.35 GPa is reached, the hydrostatic pressure remains nearly constant as the transformation occurs and the volume contracts. However, below and above this transition pressure, the stress is linearly related to the strain, as expected.

The change in the element volume can be seen in Fig. 5(b), where the normalized element volume is plotted as a function of time. The two curves represent, respectively, the case without phase transform (blue) and with the phase transform (red). Once the critical transformation pressure is reached, phase transformation occurs and a sudden decrease of 8.82% in volume is seen, indicating the occurrence of the phase transformation.

3.3. Steel fibers

The Johnson–Cook model is used to describe the behavior of the steel fibers. This model allows the rate-dependent hardening behavior of steel to be accounted for. The Johnson–Cook constitutive relation can be expressed as

$$\bar{\sigma}(\bar{\varepsilon}^p, \dot{\varepsilon}^p, T) = (A + B(\bar{\varepsilon}^p)^n)\left[1 + C \log\left(\frac{\dot{\varepsilon}^p}{\dot{\varepsilon}_0}\right)\right]\left[1 - \left(\frac{T - T_{tr}}{T_m - T_{tr}}\right)^m\right]. \tag{20}$$

Here, *A*, *B*, *C*, *m*, and *n* are material parameters that are calibrated using experimental data (Zhou et al., 2008). The first expression on the right hand side accounts for strain hardening, the second expression accounts for strain-rate hardening, and the third expression accounts for thermal softening. Model parameters are listed in Table 3. The use of the Johnson–Cook relation partly reflects the nature of the deformations analyzed and partly reflects the fact that extensive experimental data is available and has been used to calibrate the this model for the conditions analyzed. Indeed, there are more "sophisticated" models than Johnson–Cook. These models may use different parameters or internal stare variables to deal with issues such as complicated loading paths, varying stress triaxiality, and deformation mechanisms. However, the key aspects of the loading conditions analyzed in this paper are dynamic (also reflected in governing equations), rate-dependent, monotonic (no unloading considered), and approximately proportional. Under such conditions, the constitutive response of the steels considered can be well-characterized as dependent on strain, strain rate and temperature. Models using relations between stress and these quantities are effectively similar or equivalent, as long as enough parameters exist to allow a good fit to experimental data. Another way to look at it is that, for the conditions stated above, many more sophisticated models using, say, certain internal state variables (ISVs) essentially simplify to relations involving stress, strain, strain rate and temperature as independent variables.

3.4. Interfaces

Cohesive elements are specified between all bulk elements boundaries with the exception of elements in the fibers, which are assumed to undergo no fracture. The cohesive elements allow for damage initiation and development. The use of a cohesive crack zone for modeling fracture in concrete materials has a long and well-established history, dating back to the 1970s with the work by Hillerborg et al. (1976). The use of zero-thickness cohesive elements was established in 1989 by Gens et al. (1989). A bilinear

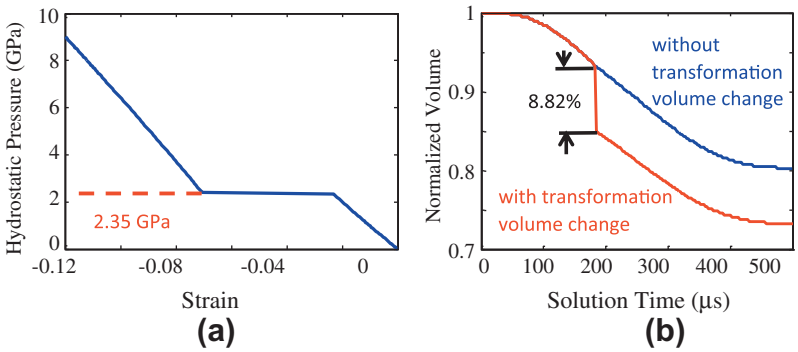

Fig. 5. Validation of the phase transformation algorithm through the consideration of the response of a unit cube under hydrostatic pressure: (a) hydrostatic pressure as a function of radial strain, and (b) unit cube volume as a function of time with and without transformation.

Table 3
Parameters used in Johnson–Cook model for reinforcing steel fibers.

Density (g/cm^3)	7.8
Young's modulus E (GPa)	203
Poisson's ratio (ν)	0.28
A (MPa)	792
B (MPa)	510
n	0.26
C	0.014
T_{room} (K)	300
T_{melt} (K)	1793
m	1.03
$\dot{\varepsilon}_0$ (s^{-1})	1
Specific heat (J/kg K)	477

traction-separation law is adopted to govern the behavior of the cohesive elements (Camanho et al., 2003). The use of a bilinear traction-separation law to model fracture in concrete materials was first formulated by Petersson (1981) in 1981 and has seen extensive use in the time since (Roesler et al., 2007). Newer relations, such as those by (Xu and Needleman (1993), Park et al. (2009), Mosler and Schneider (2011), Tomar et al. (2004), Zhai et al. (2004), potentially allow for more complete descriptions of various features. Such relations may require more parameters. Fundamentally, these relations share many common attributes, such as (1) mixed-mode nature that allows for combined normal and shear separations, and (2) control over the artificial elastic behavior introduced by the presence of cohesive elements. The cohesive traction-separation law used here possesses these attributes, while maintaining a balance between readily available material parameters and the flexibility to simulate the primarily mode II failure considered.

The linear-elastic part of the traction-separation law relates the traction vector **t** to the element stiffness **K** and the separation **u** resulting from the traction vector **t**. This relationship is given by

$$\mathbf{t} = \mathbf{K}\mathbf{u}. \tag{21}$$

The above equation can be expressed in matrix form to indicate coupling between the normal and shear components of the traction-separation relationship, i.e.,

$$\begin{pmatrix} t_n \\ t_s \\ t_t \end{pmatrix} = \begin{bmatrix} K_{nn} & K_{ns} & K_{nt} \\ K_{ns} & K_{ss} & K_{st} \\ K_{nt} & K_{st} & K_{tt} \end{bmatrix} \begin{pmatrix} u_n \\ u_s \\ u_t \end{pmatrix}. \tag{22}$$

Full coupling between normal and shear components in the traction-separation response is represented by the off-diagonal terms. For the purposes of this work, an uncoupled relation is chosen, i.e.,

$$\begin{pmatrix} t_n \\ t_s \\ t_t \end{pmatrix} = \begin{bmatrix} K_{nn} & 0 & 0 \\ 0 & K_{ss} & 0 \\ 0 & 0 & K_{tt} \end{bmatrix} \begin{pmatrix} u_n \\ u_s \\ u_t \end{pmatrix}. \tag{23}$$

Although the linear-elastic part of the response has no coupling between shear and normal components, damage initiation and evolution have a mixed-mode form. Damage initiation follows the quadratic interaction relationship shown in Eq. (24), where t_n is the normal stress in a cohesive element, t_s is the shear stress in one shear direction, t_t is the shear stress in the other in-plane shear direction, and t_n^0, t_s^0, t_t^0 are the critical values of t_n, t_s, t_t, respectively. These critical values represent the cohesive strengths for pure normal or shear separation in the corresponding directions. In this paper, t_s^0 and t_t^0 are assumed to have the same value that is different from the value of t_n^0. Because it is not physically meaningful for compressive tractions to contribute to damage initiation, only non-negative (tensile) normal tractions are considered in the damage initiation rule. This is indicated by the presence of the Macaulay brackets around t_n. Damage is initiated when

$$\left(\frac{\langle t_n \rangle}{t_n^0}\right)^2 + \left(\frac{t_s}{t_s^0}\right)^2 + \left(\frac{t_t}{t_t^0}\right)^2 = 1. \tag{24}$$

Once damage is initiated in a cohesive element, the interface follows the mixed-mode fracture criterion of Benzeggagh and Kenane given in Eq. (25) Benzeggagh and Kenane, 1996. In this relationship, G_n, G_s, and G_t are the work performed by tractions t_n, t_s, and t_t, respectively. G_n^C, G_s^C and G_t^C are the critical fracture energies in the normal and shear directions, respectively. These quantities are used to determine the degree of damage in a cohesive surface pair. For convenience, the critical fracture energies in the two shear directions are treated as equal (i.e., $G_s^C = G_t^C$). The criterion is written as

$$G_n^C + \left(G_S^C - G_n^C\right)\left(\frac{G_S + G_t}{G_n + G_S + G_t}\right)^{\eta} = G^C. \tag{25}$$

There are four interface zones in the model, i.e., paste-paste, quartz-quartz, quartz-paste, and fiber-paste. The constitutive behavior of all cohesive elements modeled in this study follows the same constitutive law; however, the calibration of the traction-separation stiffness, peak traction across the element (t_i^0), and the normal and shear fracture energies (G_n^f and G_s^f) is specific to each type of interface. The parameters for all cohesive relations used in this study are presented in Table 4. The values in the table are based on experimental data for concrete with and without fiber reinforcement (Li, 1994; Shen and Paulino, 2011). Although G_s^f has often been assigned higher values than G_n^f, these quantities have also been assigned similar values in the literature (Carpinteri et al., 1993; Fracture Mechanics of Concrete Structures, 1992). In

the calculations of this paper, failure is almost exclusively mode II (sliding under pressure); mode I does not manifest. The choice of G_n^f does not make a significant difference in the results.

As shown in Table 4, the traction-separation stiffness for cohesive elements along interfaces between the phases and within the bulk phases is 10^3 times the stiffness of the corresponding bulk elements. This choice has two benefits. First, artificial softening of the model is avoided. Second, the work of separation associated with the linear-elastic portion of the cohesive behavior is minimized, ensuring that the bulk of the work is in the fracture energy, providing adequate softening in the cohesive response. Although the method of constituent preparation can have a significant influence on the resulting composite fracture toughness (Abell and Lange, 1998), only a single set of interface properties are considered in this paper.

3.5. Interfacial contact and friction

After failure of cohesive elements, contact between bulk elements leads to frictional sliding. Contact between element faces is incorporated into the model using the a contact algorithm similar to that developed by Camacho and Ortiz (Camacho and Ortiz, 1996). The algorithm identifies free surfaces and fractured surfaces as potential contact surfaces in each time step of the simulation. Nodal coordinates at the end of every time step are used to define master and slave surfaces for the next time step. Nodal displacements are then calculated at the beginning of every time step. The corresponding nodal coordinates are used to check whether nodes of one internally defined surface have penetrated another internally defined surface. If penetration is predicted, then penalty forces of sufficient magnitude are applied to the surfaces in the direction of their normal such that there is contact between them but no interpenetration. For surfaces that are in contact, the Coulomb friction law governs the interfacial friction force. The coefficient of sliding friction for all interfaces is chosen to be 0.6, a typical value for cement-on-cement sliding (Building Code Requirements for Structural Concrete, 1995). It is assumed that the static and dynamic coefficients of friction are the same.

4. Results and discussion

To delineate the effect of the phase transformation on the response of UHPC, the results of simulations not accounting for the phase transformation (as discussed in Buck and McDowell (2012)) are compared with the results of calculations that do account for the transformation. The two sets of calculations are conducted under the same loading and constraint conditions. The former set of simulations will be referred to as the "baseline" simulations. The latter set of simulations will be referred to as the "transformation-enabled simulations".

4.1. Effect of phase transformation on load-carrying capacity

As the stress wave propagates through a microstructure, the hydrostatic pressure exceeds the threshold of 2.35 GPa behind the wave front, causing the quartz aggregate to transform into coesite as shown in Fig. 6. The particular microstructure shown contains 40% aggregate, 0% porosity, and 10% fibers by volume. Fig. 6(a) shows the microstructure at 0.5 μs. At this early stage, the stress wave has just begun to propagate through the material, only quartz at the very top of the microstructure has transformed into coesite. In Fig. 6(b), which corresponds to 3.0 μs, the stress wave has traversed approximately half the length of the structure. All quartz behind the wave front has transformed into coesite, while all the quartz ahead of the wave front remains in the α-quartz phase. Fig. 6(c) shows the microstructure at 6.0 μs, where the stress wave has almost reached the bottom surface, and essentially all quartz in the structure is in the coesite state.

The load-carrying capacity as measured in the transformation-enabled simulations is compared to that from the baseline simulations in Fig. 7. As described in the companion paper, (Buck et al., 2012), the average traction in the vertical direction on the upper surface of a microstructure at any single time step is taken to be a measure of the load carried. This figure shows four subplots, each corresponding to a different aggregate volume fraction. The horizontal axes correspond to the fiber and porosity volume fractions. The vertical axis shows the ratio of the load-carrying capacity calculated from the simulations with the quartz phase change to the load-carrying capacity from the baseline simulations without the phase change. The results show a minor downward shift in the load-carrying capacity. In particular, the load-carrying capacity calculated from the simulations with the phase change is in the range of +1.5–−10.1% of the load-carrying capacity calculated from the baseline simulations.

As Fig. 7 shows, the load-carrying capacity ratio decreases continuously as the aggregate volume fraction increases. The load-carrying capacity ratio is relatively insensitive to fiber or porosity content; that is, it is rather constant at a given aggregate volume fraction. The fact that the load-carrying capacity decreases relative to the baseline case with increasing aggregate content suggests that the phase transformation leads to more internal damage within the aggregate, which, in turn, reduces the load carried by the material. This effect is undesirable.

4.2. Effect of phase transformation on energy-dissipation capacity

4.2.1. Effect of phase transformation on total energy dissipation

The quartz phase transformation has a more significant effect on the total energy dissipation than on the load-carrying capacity. The ratio of the total energy dissipation calculated from the transformation-enabled simulations to the total energy dissipation calculated from the baseline simulations is shown in Fig. 8. For the sake of brevity, this ratio will be referred to as the "total energy ratio". The simulations with the phase transformation lead to higher energy dissipation values. Specifically, the total energy dissipation calculated from the simulations with the phase change is in the range of +0.3–+18.5% of the energy dissipation calculated from the baseline simulations. At low aggregate volume fractions, the total energy ratio is almost unity, indicating that the energy dissipation has not changed appreciably. However, as the aggregate

Table 4
Parameters for cohesive surfaces.

Material	Cement	Quartz aggregate	Cement-aggregate interface	Cement-fiber interface
K_n (TPa)	22.9	96.6	22.9	22.9
$K_{s/t}$ (TPa)	9.5	44.7	9.5	9.5
t_n^0 (MPa)	40.0	50.0	10.0	10.0
$t_{s/t}^0$ (MPa)	25.0	40.0	6.0	6.0
G_n^c (J/m^2)	40.0	15.0	5.0	5.0
$G_{s/t}^c$ (J/m^2)	40.0	15.0	5.0	5.0
η	1.45	1.45	1.45	1.45

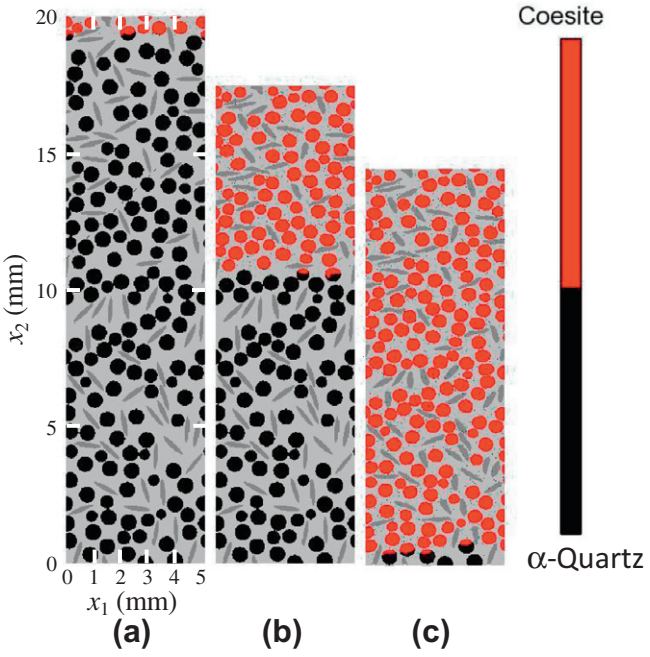

Fig. 6. Phase transition of quartz aggregate as deformation progresses at: (a) 0.5 μs, (b) 3.0 μs, and (c) 6.0 μs.

volume fraction increases, the energy dissipation relative to the baseline increases. At 10% aggregate, the maximum energy ratio is 1.03. At 20% aggregate, the maximum total energy ratio is 1.08. At 30% aggregate, the maximum total energy ratio is 1.12. At 40% aggregate, the maximum energy ratio is 1.20. This suggests that the transformation of the aggregate enhances various mechanisms of energy dissipation, as increasing aggregate levels lead to increasing energy dissipation relative to the baseline cases. This will be analyzed in more detail in subsequent sections when the contributions from different mechanisms to the total energy dissipation are considered individually.

At a given aggregate volume fraction, the effects of fibers and porosity on the total energy ratio are more complex than the relationship seen in the load-carrying capacity ratio. Note in Fig. 8(a) that at 10% aggregate, the energy dissipation ratio is relatively constant over all porosity and fiber volume fractions. In contrast, Fig. 8(d), which corresponds to an aggregate volume fraction of 40%, the energy dissipation ratio is still relatively constant at a given porosity level, but increasing the porosity decreases the ratio. Since the only difference between the two simulations is the treatment of the quartz aggregate, it would be natural to think that only the aggregate volume fraction should change the results. However, the fact that increasing porosity decreases the energy dissipation relative to the baseline cases indicates that there is a coupling between the porosity volume fraction and the quartz phase transformation. In particular, low porosity volume fractions yield a higher total energy dissipation than that of the baseline case, while high porosity volume fractions decrease the additional energy dissipation induced by the phase transformation. Although the highest porosity volume fraction considered in this study, 5%, still produces a total energy ratio above unity, the foregoing discussion suggests that there is a porosity volume fraction at which the total energy ratio is exactly one. Such a result may conceal the fact that the quartz phase transformation leads to more fracture and friction within the aggregate phase.

The quartz phase transformation introduces a new component of energy dissipation. When the phase transformation initiates, the volume of the quartz aggregate reduces. This reduction in volume is an energy-consuming process. The energy dissipated through this mechanism is related to the volume of the aggregate

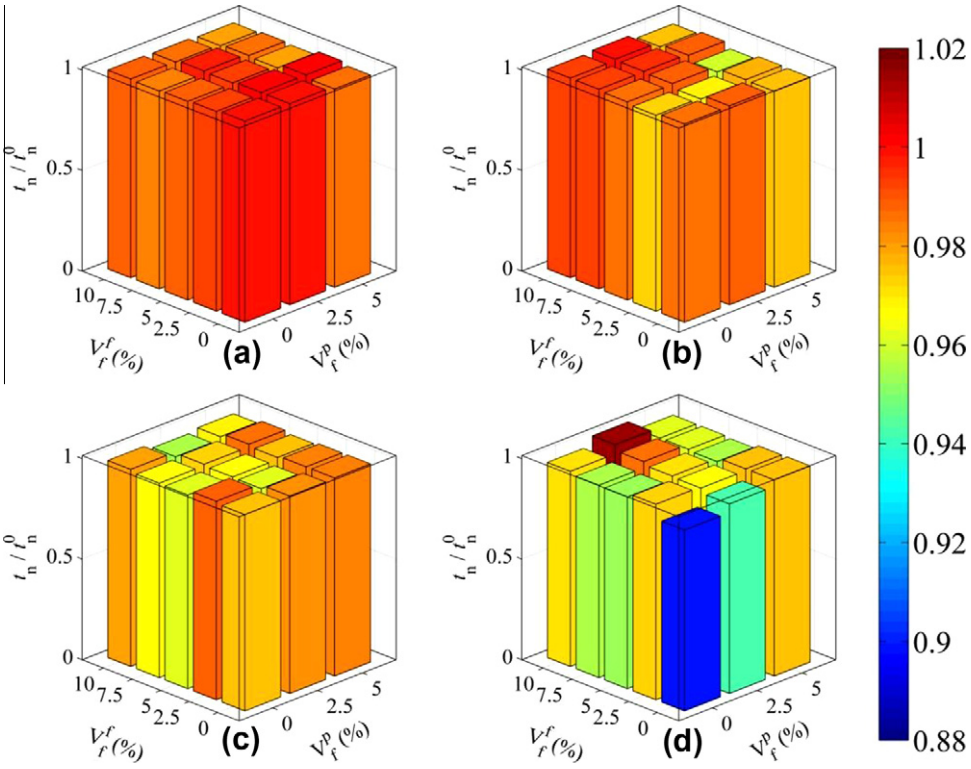

Fig. 7. Ratio between the load-carrying capacity for cases with quartz phase transformation and the load-carrying capacity for cases without transformation (baseline cases) for microstructures with (a) 10% aggregate, (b) 20% aggregate, (c) 30% aggregate, and (d) 40% aggregate.

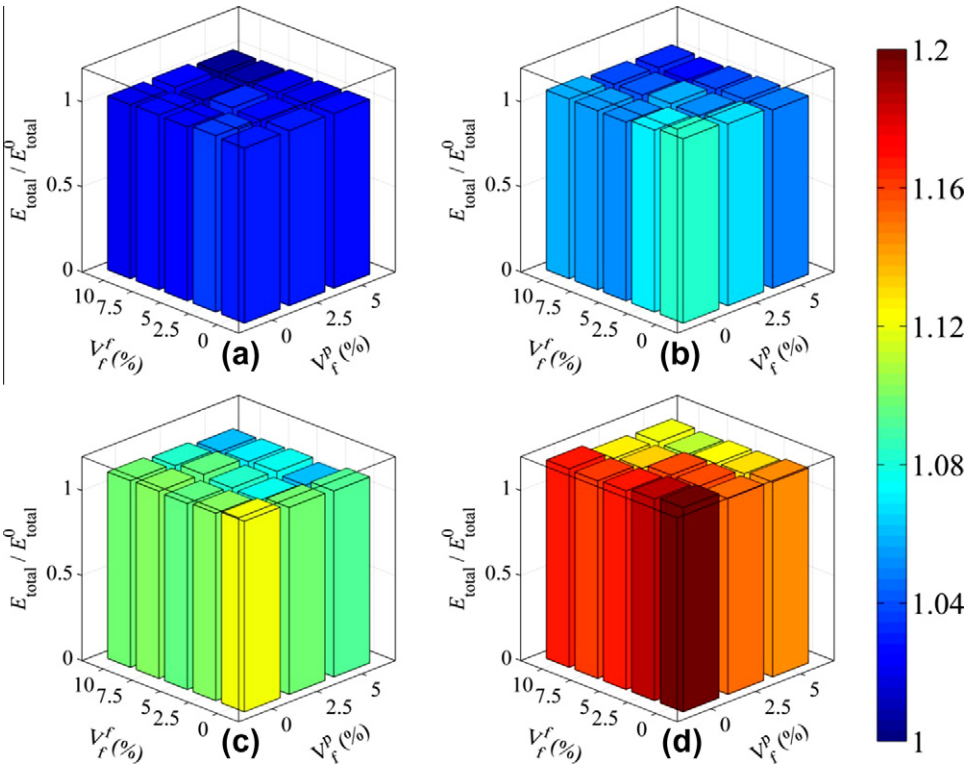

Fig. 8. Ratio between total energy dissipation for cases with quartz phase transformation and the total energy dissipation for cases without transformation (baseline cases) for microstructures with (a) 10% aggregate, (b) 20% aggregate, (c) 30% aggregate, and (d) 40% aggregate.

that has undergone transformation, the change in volume, and the threshold pressure of transformation. This component is included along with interface damage, friction, and inelastic deformation in the computation of the total energy dissipation. The magnitudes of these four energy dissipation modes relative to each other will be discussed further in the next section.

4.2.2. Effect of phase transformation on energy dissipation modes

This section considers how the quartz phase transformation affects the contributions of different mechanisms to the total dissipation over the course of the deformation process. Subsequent sections will consider the effect of phase transformation on the individual energy dissipation modes. Fig. 9 shows the evolution of the energy dissipation modes in a microstructure with 40% aggregate, 0% porosity, and 0% fibers. The subscripts *d*, *p*, *f*, and *tr* refer to energy dissipated through damage, plasticity, fracture, and phase transformation, respectively. Recall that this microstructure provides the highest total energy dissipation ratio (see Fig. 8). Fig. 9(a) corresponds to the simulation with the quartz phase transformation, while Fig. 9(b) corresponds to the simulation without the phase transformation. It can be seen that, as compared to the simulation that does not account for phase transformation, the results of the transformation-enabled simulation show a larger percentage of energy dissipation due to friction, and less due to inelastic deformation. In particular, friction accounts for 36.9% of the total energy dissipation and inelastic deformation accounts for 62.3% of the total energy dissipation in the transformation-enabled simulation. In the baseline simulation, friction accounts for 20.6% of the total energy dissipation, and inelastic deformation accounts for 79.2% of the total energy dissipation. In both cases, the energy dissipated through interface damage and fracture is less than 0.5%. However, differences are evident. Interface damage and fracture dissipates 0.29% of the total energy imparted into the material by the applied load in the transformation-enabled simulation, whereas dissipation through interface damage and fracture constitutes only 0.13% of the total energy input in the baseline simulations. Because the loading and constraint conditions are identical in all cases, an increase in frictional dissipation is not possible without an increase in interface fracture. Clearly, then, the quartz phase transformation does not lead merely to more interface damage alone, but also leads to a higher crack density. This increased crack density then gives rise to the significant increase in energy dissipation discussed previously. This will be further analyzed in the next section.

Fig. 9(a) also shows the energy dissipated through phase transformation of the quartz aggregate for a microstructure with 40% aggregate, 0% porosity, and 0% fibers. At 6.0 μs, the phase transformation contributes less than 1.5% of the total energy dissipation. All other microstructures show even smaller proportions of energy dissipated through phase transformation. Although the transformation itself dissipates a relatively small amount of energy, it induces substantially higher energy dissipation by enhancing other dissipation mechanisms. This will be quantified in the next three sections that address the three mechanisms of interface damage, interface friction, and inelastic deformation individually.

Further insight into the relationships between the phase volume fractions, the quartz phase transformation, and energy dissipation can be gained by considering the three components of energy dissipation.

4.2.3. Effect of phase transformation on energy dissipated through interface damage and fracture

Fig. 10 shows the ratio of the energy dissipation through interface damage in the transformation-enabled simulations to that of the baseline simulations. For the sake of brevity, this ratio will be referred to as the "damage dissipation ratio". In all microstructures, the damage energy ratio is higher than one, indicating that the phase transformation leads to greater frictional dissipation.

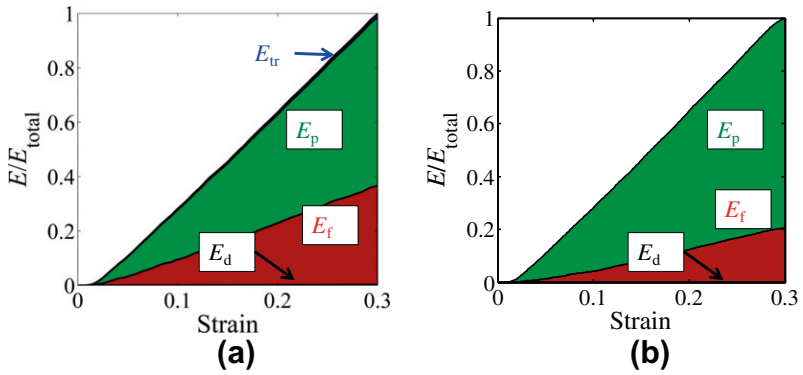

Fig. 9. Evolution of the energy dissipated through different mechanisms in a microstructure with 40% aggregate, 0% porosity, and 0% fibers for simulations (a) with quartz phase transformation and (b) without quartz phase transformation.

The quartz phase transformation has a strong effect on the energy dissipated via interface damage and fracture. The phase transformation yields damage dissipation levels that are up to 94.0% higher than those of the baseline cases.

Aggregate and porosity have competing effects on the damage dissipation ratio, and this trend becomes more pronounced at higher aggregate volume fractions. At 10% aggregate and 0% fibers, decreasing the porosity from 5% to 0% increases the damage energy ratio from 1.13 to 1.23, giving a net change of 0.1. At 40% aggregate and 0% fibers, decreasing the porosity from 5% to 0% increases the damage energy ratio from 1.52 to 1.87, a net change of 0.35. The highest ratios are seen at an aggregate volume fraction of 40% and a porosity volume fraction of 0%. The lowest ratios are seen at an aggregate value fraction of 10% and a porosity volume fraction of 5%.

The trends in the damage dissipation ratio bear resemblance to the trends in the total energy dissipation ratio. Both ratios increase with increasing aggregate fraction. Both ratios are negatively affected by the porosity volume fraction, and the influence of porosity becomes more pronounced at high aggregate volume fractions. The underlying cause for the coupling between aggregate and porosity can be determined by looking at the energy dissipated through damage and fracture along different types of interfaces.

Fig. 11 shows the energy dissipated through damage and fracture of the cement phase, fracture of the quartz phase, and debonding along the cement-quartz interfaces in microstructures with 40% aggregate, and 0% fibers. The top row, i.e., Fig. 10(a) and (b), corresponds to microstructures with 0% porosity. The bottom row, i.e., Fig. 10(c) and (d), corresponds to microstructures with 5% porosity. The left column, i.e., Fig. 10(a) and (c),

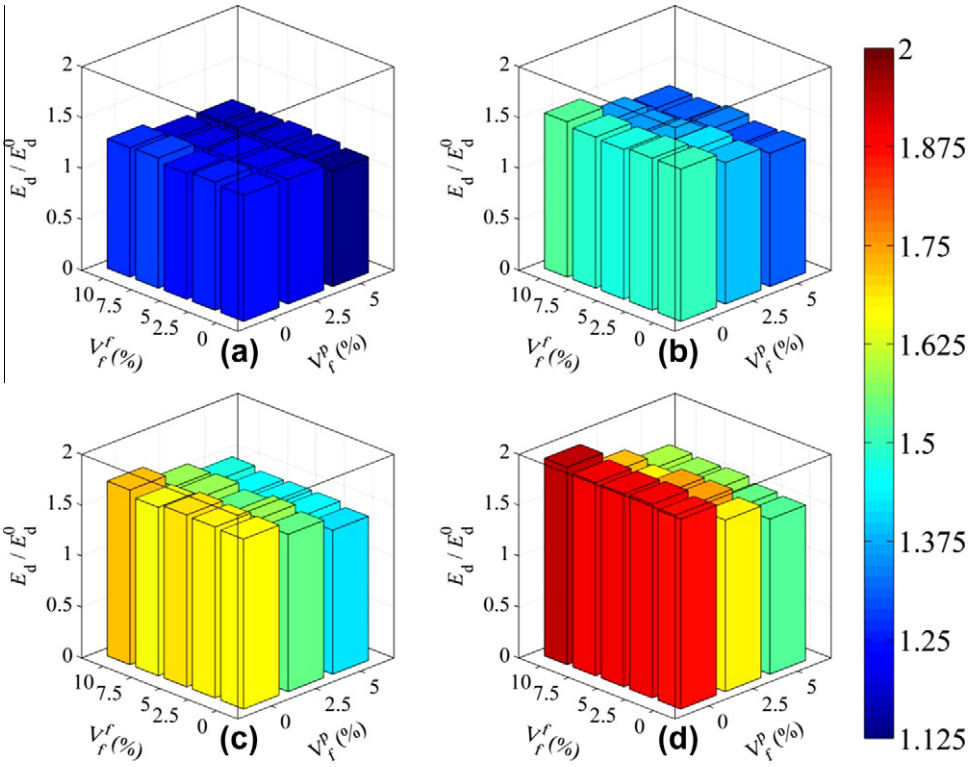

Fig. 10. Ratio between the energy dissipated through damage for cases with quartz phase transformation and the energy dissipated through damage for cases without the phase transformation (baseline cases) for microstructures with (a) 10% aggregate, (b) 20% aggregate, (c) 30% aggregate, and (d) 40% aggregate.

corresponds to cases without the quartz phase transformation. The right column, i.e., Fig. 10(b) and (d), corresponds to cases with the quartz phase transformation. First, consider the left column. Without the phase transformation, damage and fracture within the cementitious matrix and quartz aggregate comprise roughly half of the overall damage dissipation regardless of the porosity level. In particular, at 0% porosity, damage dissipation within the cementitious matrix and quartz aggregate constitute 51.2% and 47.8%, respectively, of the overall damage dissipation. At 5% porosity, damage dissipation within the cementitious matrix and quartz aggregate constitute 52.0% and 47.1%, respectively, of the overall damage dissipation. Clearly, the porosity does not have an appreciable influence on the locations of interface damage in the absence of the phase transformation. Now consider the right column. At 0% porosity, a much larger proportion of the damage dissipation is attributable to intra-quartz fracture with the phase transformation. Specifically, 72.1% of the total is attributable to fracture surfaces inside the quartz phase, while only 27.2% is attributable to fracture surfaces within the cementitious matrix. Also, note that increasing porosity lowers the fraction dissipation attributable to the quartz aggregate. At 5% porosity, damage and fracture within the quartz aggregate drops to 65.1% of the total, while damage and fracture dissipation within the cementitious matrix increases to 34.2% of the total. Since increasing the porosity decreases the damage dissipation ratio, as seen in Fig. 10, the shift cannot be simply due to increased damage and fracture within the cementitious matrix resulting from higher porosity when phase change is considered. Rather, the shift is due to the lower stresses in the quartz aggregate at higher porosity levels. Such lower stresses make transgranular fracture less likely. A look at the crack density provides more insight in this regard.

In this paper's companion work (Buck et al., 2012), the crack density is used to quantify the extent of cracking within the UHPC microstructures. The same technique is used in the transformation-enabled simulations. Due to the complexity in comparing the two-dimensional crack density tensor among microstructures with three constituent phases, the scalar crack density parameter is used to assess the influence of the quartz phase transformation on the extent of cracking. Fig. 12 shows the ratio of the scalar crack density parameter in the transformation-enabled simulations to the scalar crack density parameter in the baseline simulations. At all aggregate volume fractions, the case with phase transformation has at least twice the amount of cracking than the case without phase transformation. At high fiber volume fractions and low porosity volume fractions, the case with phase transformation leads to almost five times the amount of cracking than the case without transformation. As the porosity volume fraction increases, the crack density ratio decreases, even for large fiber volume fractions. This trend is similar to the trend observed in the damage energy dissipation ratio. This indicates that increasing the porosity volume fraction brings the amount of cracking in the baseline and transformation-enabled simulations closer together. In other words, increasing the porosity volume fraction provides stress relief within the quartz aggregate, leading to less cracking within the quartz aggregate than would otherwise occur at lower porosity levels.

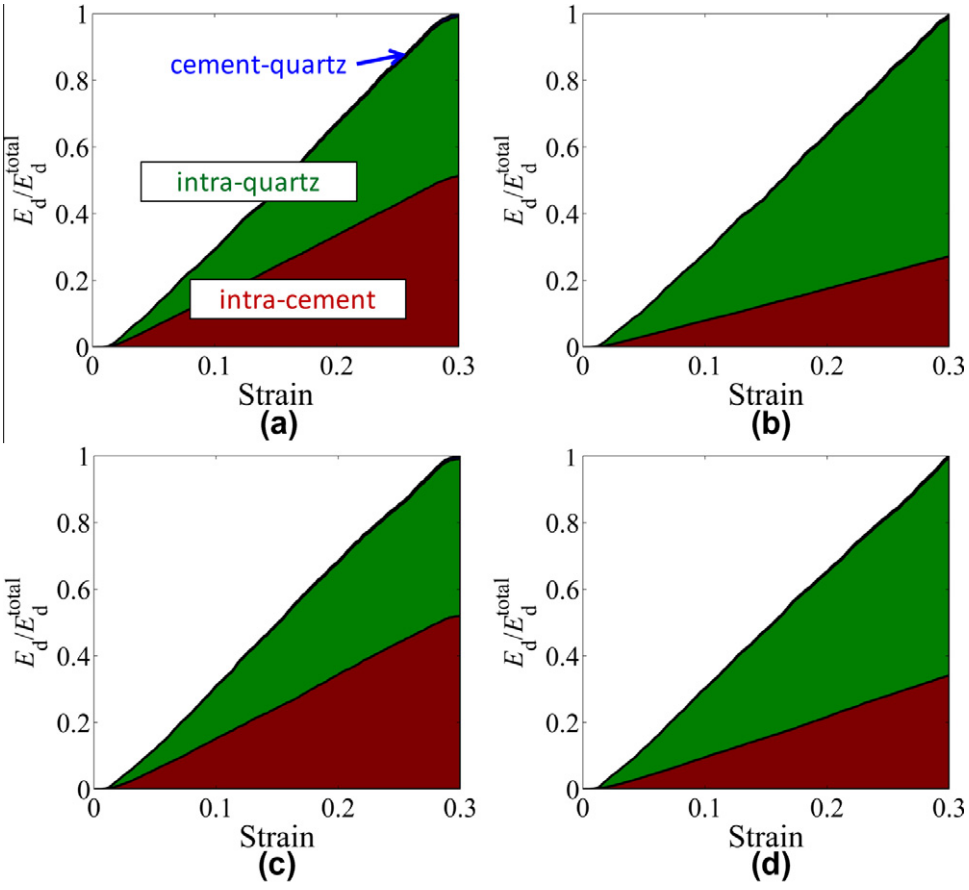

Fig. 11. Fraction of energy dissipated through damage and fraction of energy dissipated through fracture (intra-cement, intra-quartz, and along cement-quartz interfaces) in microstructures with 40% aggregate, 0% fibers, and (a) 0% porosity without phase transformation, (b) 0% porosity with phase transformation, (c) 5% porosity without phase transformation, and (d) 5% porosity with phase transformation.

4.2.4. Effect of phase transformation on energy dissipated through friction between fractured interfaces

The ratio of the frictional energy dissipation calculated from the transformation-enabled simulations to the frictional energy dissipation calculated from the baseline simulations is shown in Fig. 13. For the sake of brevity, this ratio will be referred to as the "friction energy dissipation ratio". The quartz phase transformation has a drastic effect on the energy dissipated through friction between fractured interfaces. In particular, the phase transformation yields frictional energy dissipation levels that are up to 113% higher than those of the baseline simulations. The trends in the friction energy ratio bear resemblance to the trends in the damage energy ratio. The friction energy ratio increases with increasing aggregate content and decreasing porosity content. However, there is one exception to the similarities with the damage energy ratio. In the previous section, the damage energy ratio is independent of the fiber volume fraction. In this case, higher fiber volume fractions tend to decrease the friction energy ratio.

There is a competition between the effects of aggregate and fibers on the friction energy ratio. The influence of fibers is most pronounced at low aggregate volume fractions. For example, at 10% aggregate and 0% porosity, increasing the fiber volume fraction from 0% to 10% decreases the friction energy ratio from 1.77 to 1.34. In contrast, at 40% aggregate, increasing the fiber volume fraction from 0% to 10% only decreases the friction energy ratio from 2.13 to 2.07. This suggests that at low aggregate volume fractions, fibers can effectively reduce the increase in frictional dissipation caused by the quartz phase transformation. However, at high aggregate volume fractions, increasing the fibers has only a minimal effect on the frictional dissipation enhancement due to the phase transformation.

It is instructive to note that dissipation along crack faces and dissipation within the bulk constituents do not occur independently. The relative magnitudes of the different forms of dissipation may be different if, say, the material constitutive relation is changed. In particular, an uncapped Drucker–Prager relation is used here for the cementitious matrix and the aggregate. If a capped model is used instead, quantifications different from what is reported here may be obtained. In the model of this paper, both shear failure and crushing failure within the bulk matrix material are considered. Crushing can occur through the collapse of voids/porosity 100 μm in size at different volume fractions – these voids are explicitly modeled, i.e., there are no finite elements in the regions of the voids. Only pores below this size are implicitly considered in the Drucker–Prager constitutive relation. It would be interesting and worthwhile in the future to study how different forms of dissipation change as material constitutive behavior or relation is changed (e.g., a capped Drucker–Prager relation is used). Here, we focus on a framework for establishing microstructure-performance relations, as detailed in Section 4.3 below, with a particular set of constitutive relations.

4.2.5. Effect of phase transformation on energy dissipated through inelastic deformation

The ratio of the inelastic energy dissipation calculated from the transformation-enabled simulations to that as calculated from the baseline simulations is shown in Fig. 14. For the sake of brevity, this ratio will be referred to as the "inelastic dissipation ratio". The quartz phase transformation can decrease the energy dissipated through inelastic deformation by up to 9.3% compared to the baseline results. At a given aggregate volume fraction, the inelastic dissipation ratio is highest at low porosity volume fractions and high fiber volume fractions. In particular, the highest inelastic dissipation ratio of 0.99 is at 10% aggregate, 0% porosity, and 7.5% fibers. The lowest is seen at 40% aggregate, 5% porosity, and 0% fibers.

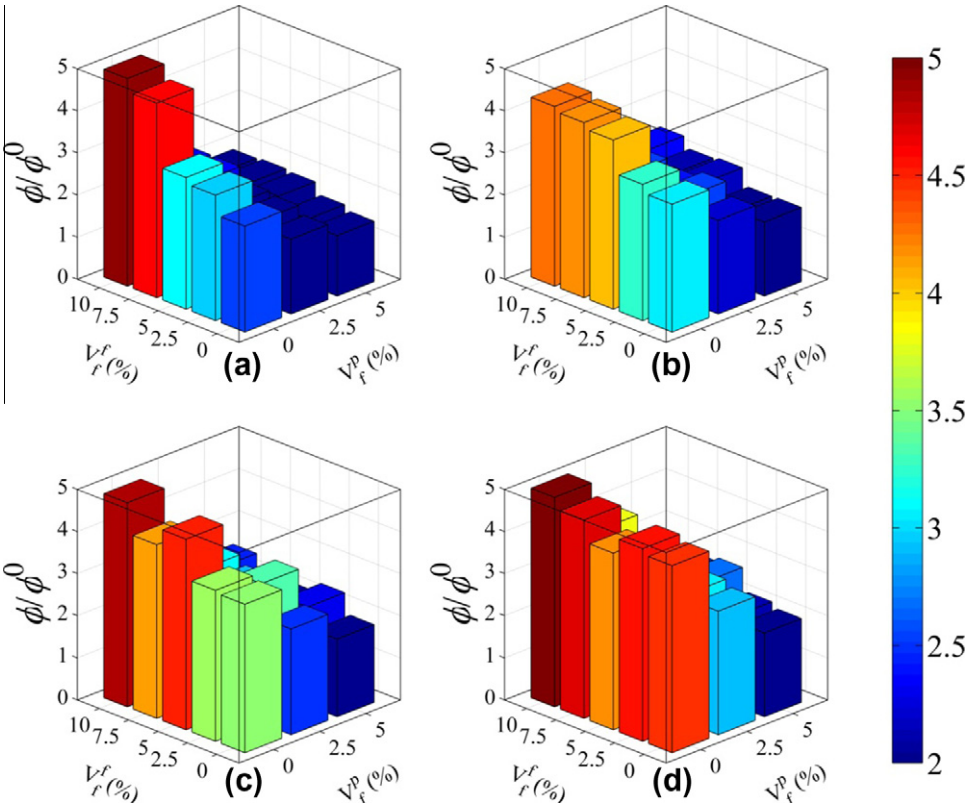

Fig. 12. Ratio of scalar crack density parameter between simulations accounting for quartz phase transformation and the baseline simulations without the phase transformation; (a) 10% aggregate, (b) 20% aggregate, (c) 30% aggregate, and (d) 40% aggregate.

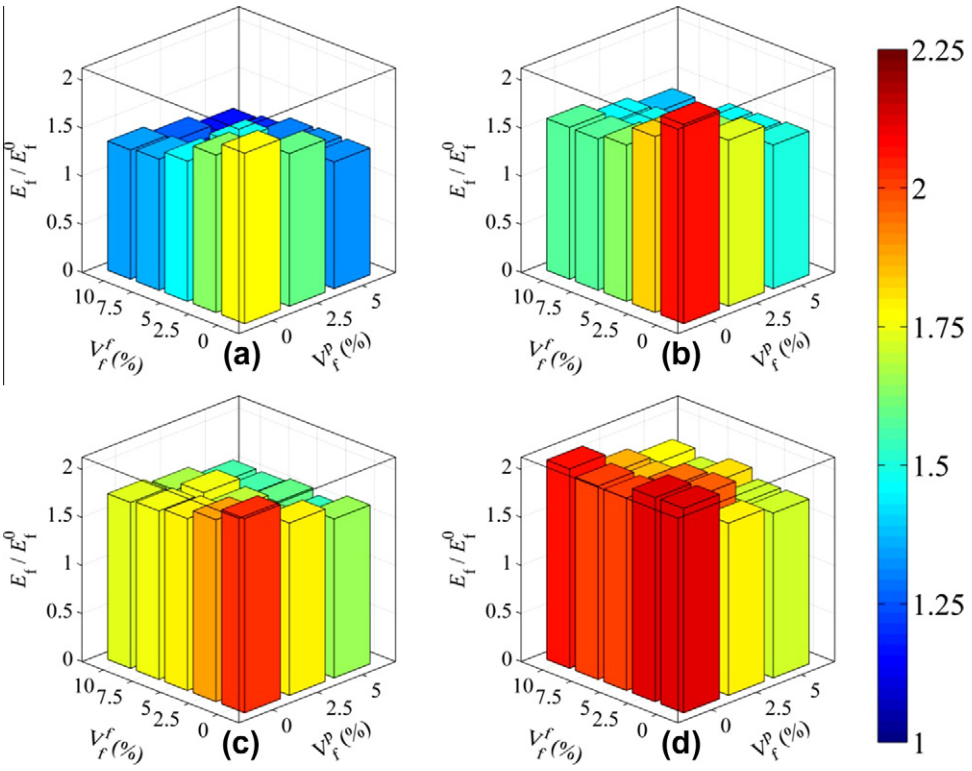

Fig. 13. Ratio of energy dissipated through interfacial friction between simulations accounting for quartz phase transformation and baseline simulations without the phase transformation; (a) 10% aggregate, (b) 20% aggregate, (c) 30% aggregate, and (d) 40% aggregate.

Note that at a given aggregate and fiber volume fraction, larger porosity volume fractions lead to lower inelastic dissipation ratios. This suggests that, in the absence of the quartz phase transformation, increasing the porosity leads to more plastic dissipation compared with the case without transformation.

Overall, the phase transformation enhances energy dissipation. This is a desirable effect in applications such as infrastructure protection or blast mitigation. This effect is opposite to the effect of the transformation on the load-carrying capability discussed earlier. Obviously, the competing effects often require a tradeoff

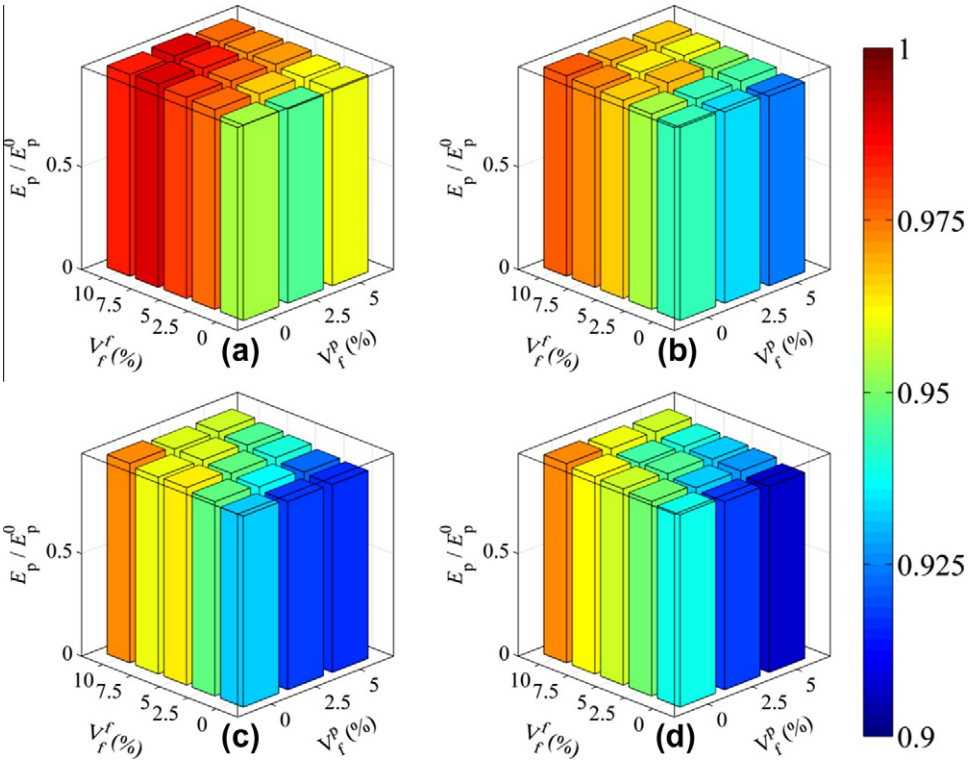

Fig. 14. Ratio of energy dissipated through inelastic deformation between simulations accounting for quartz phase transformation and baseline simulations without the phase transformation; (a) 10% aggregate, (b) 20% aggregate, (c) 30% aggregate, and (d) 40% aggregate.

which can only be reached through systematic and quantitative relations between material microstructure and performance parameters as discussed below.

4.3. Microstructure-performance relation maps

In the first part of this study (Buck et al., 2012), a set of microstructure-performance relation maps that relate the volume fractions of the constituents to the load-carrying and energy-dissipation capacities are developed. Such structure–property/response maps provide quantification that can be used in top-down materials' design, where performance objectives are specified and the necessary material attributes are then identified. An updated microstructure-performance relation map is shown in Fig. 15 that accounts for the effects of the quartz phase transformation. To facilitate comparison with the relations developed without consideration of the phase transformation, the results of η_1, η_2, and η_3 are superimposed over Fig. 15(a)–(c), respectively. In Fig. 15(a) the

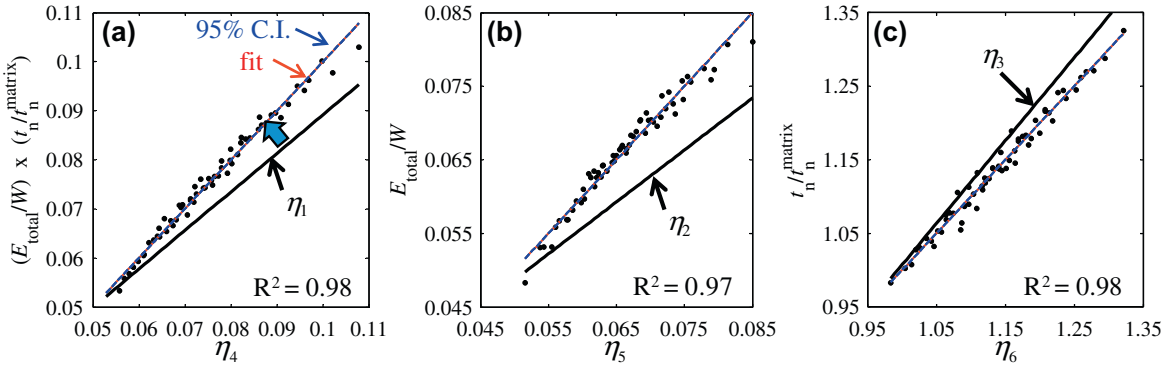

Fig. 15. Microstructure-performance relation map relating (a) energy-dissipation and load-carrying capacities to volume fractions of constituents, (b) energy-dissipation capacity to volume fractions of constituents, and (c) load-carrying capacity to volume fractions of constituents.

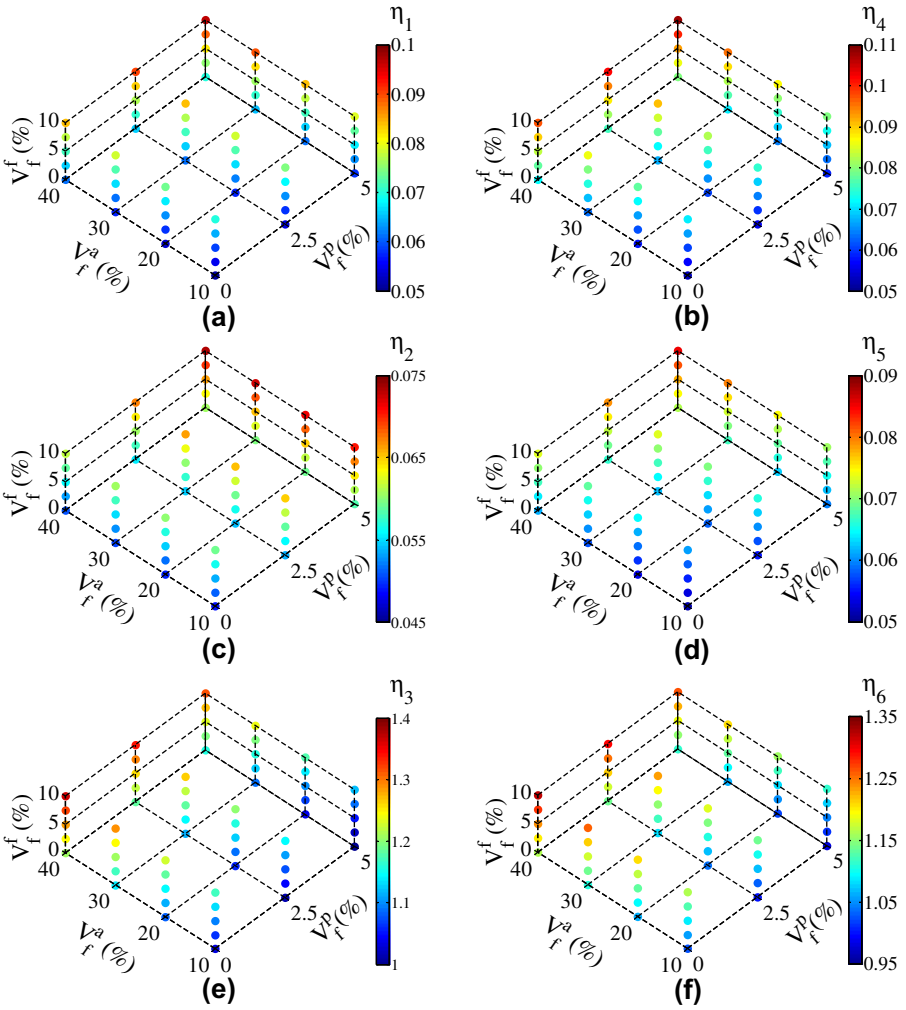

Fig. 16. Values of performance parameters shown over the microstructure design space: (a) η_1, (b) η_2, (c) η_3, (d) η_4, (e) η_5, and (f) η_6.

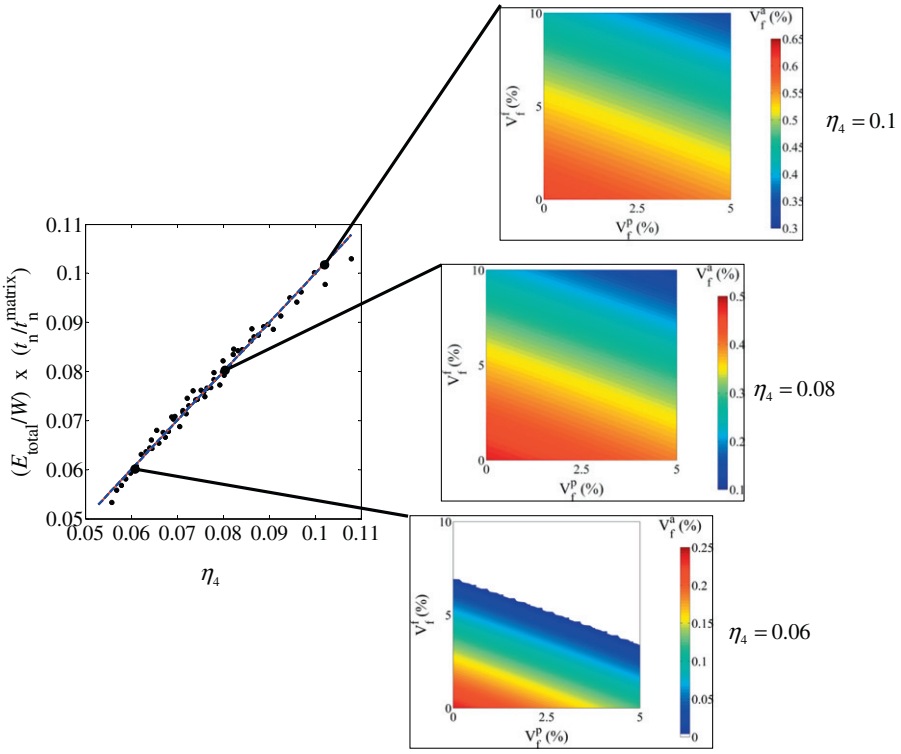

Fig. 17. Constituent volume fractions that satisfy three different values of the combined performance parameter η_4.

vertical axis shows a combined performance metric defined as the product of the energy-dissipation capacity and the load-carrying capacity. Here, the energy-dissipation capacity is expressed as the total energy dissipation normalized by the total external work; that is, the total work dissipated as a fraction of the total work imparted into the material. The load-carrying capacity is expressed as the traction on the upper surface of a given microstructure normalized by the traction on the upper surface of a microstructure comprised of 100% cementitious matrix. The horizontal axis is a parameter that depends on the traction carried by the material and the volume fractions of the constituents in microstructures. This parameter is obtained through a linear regression analysis and takes the form of

$$\left(\frac{E_{Total}}{W}\right) \times \left(\frac{t_n}{t_n^{matrix}}\right) = \eta_4 = \frac{0.049}{\left(1 - V_f^a\right)^{0.76}\left(1 - V_f^f\right)^{2.8}\left(1 - V_f^p\right)^{2.1}}, \quad (26)$$

which provides the best description of the correlation among dissipation, loading carried, and microstructure. In the above relation, as well as in Eqs. (27) and (28) below, V_f^a, V_f^f, and V_f^p refer to the volume fractions of aggregate, fibers, and porosity, respectively. The chart in Fig. 15(a) can be used to select a desired microstructure setting for any given combination of load-carrying capacity and energy-dissipation capacity. The relations also illustrate the trade-offs between energy dissipation and strength in microstructure design. Fig. 15(b) relates the energy-dissipation capacity to the volume fractions of constituents. The parameter that provides the best description of the correlation between the dissipation and microstructure is

$$\frac{E_{Total}}{W} = \eta_5 = \frac{0.049}{\left(1 - V_f^a\right)^{0.45}\left(1 - V_f^f\right)^{1.6}\left(1 - V_f^p\right)^{2.9}}. \quad (27)$$

Fig. 15(c) relates the load-carrying capacity to microstructure. The parameter that provides the best description of the correlation between the load carried and microstructure is

$$\frac{t_n}{t_n^{matrix}} = \eta_6 = \frac{0.99\left(1 - V_f^p\right)^{0.81}}{\left(1 - V_f^a\right)^{0.45}\left(1 - V_f^f\right)^{1.6}}. \quad (28)$$

The relations in Eqs. (26)–(28) correspond to the design space for which the ranges of the input variables are $10\% \leqslant V_f^a \leqslant 40\%$, $0\% \leqslant V_f^f \leqslant 10\%$, and $0\% \leqslant V_f^p \leqslant 5\%$. These microstructure-performance relations bear many similarities to those presented in the first part of this study (Buck et al., 2012). A key difference is that in the first part (Buck et al., 2012), η_1 (which corresponds to η_4 here) has exponents of 0.47, 3.0, and 2.6 for the aggregate, fiber,

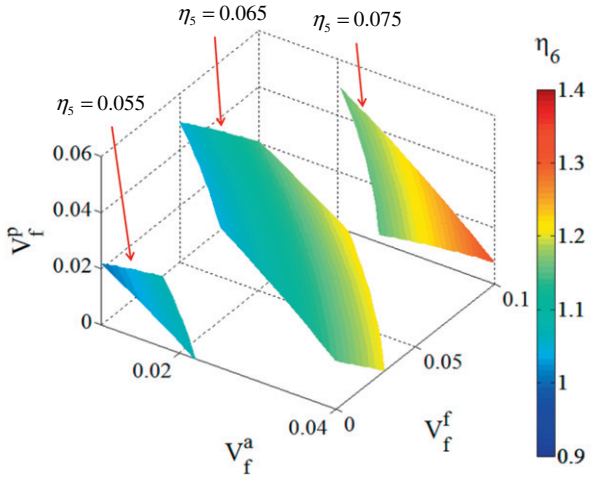

Fig. 18. Isosurfaces for the η_5 parameter with shading indicating the value of the η_6 parameter within the design space used in this study.

and porosity phases, respectively. This illustrates that the phase transformation alters the significance of the aggregate and porosity in the dynamic response of UHPC, while the significance of the fibers is relatively independent of the transformation. This difference demonstrates that the phase transformation lends the aggregate a much stronger influence on energy dissipation and should be accounted for in the design of UHPC structures to better mitigate the threats of dynamic loading with high pressures.

Fig. 15(a) shows that for a given level of energy-dissipation and load-carrying capacity, a larger value of η_1 is required as compared to η_4. A similar trend can be observed in Fig. 15(b). In Fig. 15(c), for a given load-carrying capacity, a larger value of η_6 is required as compared to η_3. Because of the nature of the parametric expressions, the relationship between volume fractions of the constituents and the parameters is not one-to-one. That is, multiple microstructural compositions can yield the same parameter value. Fig. 16 shows the values of the microstructure performance parameters taken on by the whole range of microstructure instantiations analyzed. Each point in Fig. 16(a)–(f) represents one of the 60 unique combinations of volume fractions of the constituents. The color of each point corresponds to the value of the parameter as indicated by the color scale legend. The lowest values of η_1 and η_4 are seen at low volume fractions of aggregate, fibers, and porosity. Microstructures with high aggregate, high fiber, and low porosity contents show parameter values similar to microstructures with high aggregate, low fiber, and high porosity contents. Parameters η_2 and η_5 show similar relationships. Microstructures with high aggregate and high fiber volume fractions show the highest values of η_3 and η_6 with only a minor influence from porosity. Microstructures with low aggregate and low fiber volume fractions show the lowest values of η_3 and η_6. Finally, similar to what is discussed in Buck and McDowell (2012) for η_1, η_2, and η_3, the parameters η_4, η_5, and η_6 are not fully independent of each other. The parameter η_4 is approximately equal to the product of η_5 and η_6, i.e., $\eta_4 \approx \eta_5\eta_6$. This correlation provides insight and a means for analyzing the trade-offs between the competing performance metrics.

The observation that multiple microstructural compositions can yield the same performance parameter value is shown in more detail in Fig. 17. This figure illustrates how different combinations of the constituent volume fractions can yield the same performance parameter η_4. In the surface plots shown in the figure, any combination of constituent volume fractions shown on a single plot will provide a fixed parameter value as indicated. The region in white in the plot for $\eta_4 = 0.06$ is not physically meaningful, as aggregate volume fractions greater than zero are mathematically required. At all η_4 values, changes in the constituent volume fractions have the same influence on the performance parameter.

It should be emphasized that the performance parameters obtained through the relations in Eqs. (14)–(16) are valid only for the ranges of volume fractions considered ($10\% \leqslant V_f^a \leqslant 40\%$, $0\% \leqslant V_f^f \leqslant 10\%$, and $0\% \leqslant V_f^p \leqslant 5\%$). The advantage of systematically investigating the behavior of UHPC over a wide range of constituent volume fractions is that a wide range of possible performance can be obtained. More importantly, the interplays between different factors can be revealed. Fig. 18 shows a series of isosurfaces for η_5 within the 3D design space considered. Across any single surface, the value of η_5 remains constant. The shading indicates how η_6 changes even as η_5 remains constant. This figure shows that if the desired energy dissipation is specified, the load-carrying capacity can be optimized without altering the energy-dissipation parameter. A similar figure is shown in Fig. 19, which switches the position of the two parameters. This figure shows isosurfaces for η_6 with the contour shading corresponding to η_5. This figure shows that if the desired load-carrying capacity is specified, the energy-dissipation capacity can be optimized without altering the load-carrying capacity parameter.

Because the equations for the performance parameters are only valid for the range of constituent volume fractions considered ($10\% \leqslant V_f^a \leqslant 40\%$, $0\% \leqslant V_f^f \leqslant 10\%$, and $0\% \leqslant V_f^p \leqslant 5\%$), the parameters themselves are bounded. This is shown in Fig. 20, which outlines all possible combinations of η_5 and η_6 for the constituent volume fractions considered. Values of the two performance parameters lying off the solid color region are not attainable with microstructural compositions within the design space considered. The shading of the color region in the figure corresponds to the value of the combined performance parameter η_4. Because η_4 is the product of η_5 and η_6, η_4 is clearly larger when the two individual parameters are larger. However, it is impossible to maximize both η_5 and η_6 within the bounds of the design space considered. If the maximum value of η_6, roughly 1.32, is chosen, then a suboptimal value of η_5 must be accepted. Conversely, if the maximum value of η_5, roughly 0.085, is chosen, then a suboptimal value of η_6 must be accepted.

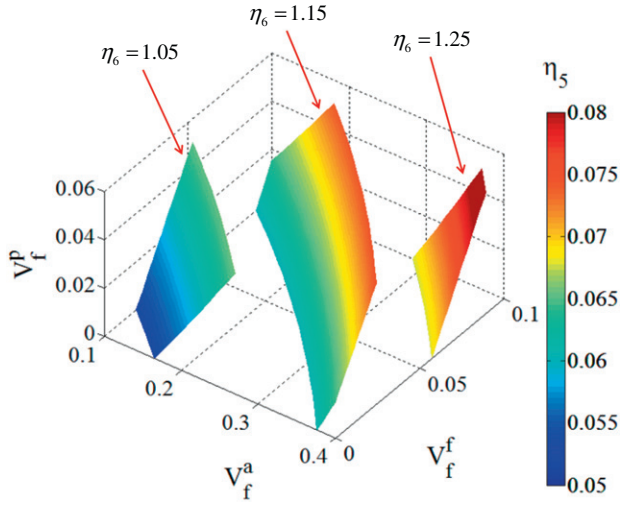

Fig. 19. Isosurfaces for the η_6 parameter with shading indicating the value of the η_5 parameter within the design space used in this study.

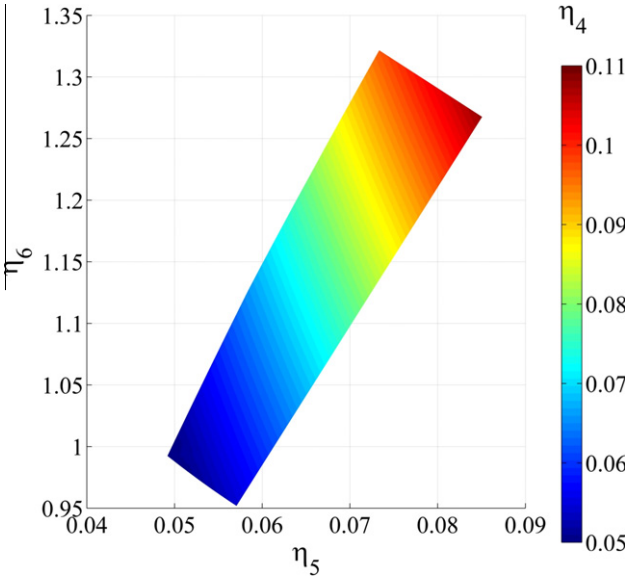

Fig. 20. Boundaries of η_5 and η_6 for the range of constituent volume fractions considered in this study.

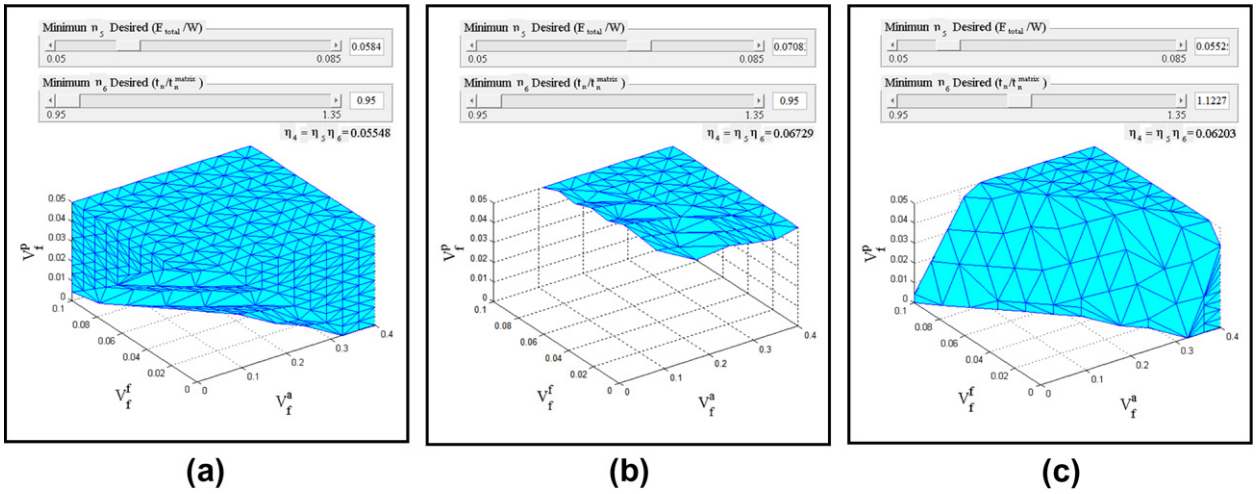

Fig. 21. Illustration of a microstructure design tool based on the Inductive Design Exploration Method (IDEM) that allows users to select the performance parameters independently and shows the portion of the design space that meets or exceeds the specified performance criteria for (a) $\eta_4 = 0.0584$ and $\eta_6 = 0.95$, (b) $\eta_4 = 0.07083$ and $\eta_6 = 0.95$, (a) $\eta_4 = 0.05525$ and $\eta_6 = 1.1227$.

Finally, the microstructure-performance relations is used in a framework incorporating the Inductive Design Exploration Method (IDEM) (Choi et al., 2008) to provide a tool that can be used to identify allowable material designs (sets of constituent volume fractions constituting permissible input space) that satisfy a given set of performance criteria (i.e., a given output space). An illustration of this tool is shown in Fig. 21. Using this tool, a user can select the two performance parameters η_5 and η_6 independently of the other, the design software will identify and display microstructural settings meeting or exceeding the desired performance criteria, i.e., having performance parameters η_5 and η_6 that are equal to or higher than the prescribed values.

5. Conclusions

Dynamic loading can give rise to elevated temperatures and high pressures. In complex heterogeneous material systems such as UHPC, the responses of the constituents to input with high temperatures and pressures and the composition of the material combine to determine the overall behavior of the material. In particular, phase transformations induced by high pressures can significantly change the overall behavior of the heterogeneous materials. Proper accounting of such phase transformations can allow materials design to take advantage of these mechanisms in order to tailor structural response for specific load applications. Studies reported in this paper have yielded a phenomenological model that accounts for the effects of the transformation of α-quartz into coesite on the behavior of UHPC. This phenomenological model is employed within the framework of a cohesive finite element model to quantify the relations between the load-carrying and energy-dissipating capacities of microstructures with different volume fractions of phases. The quantification covers a range of the microstructure parameters. In addition to yielding microstructure-response relations that can be used in materials design and selection, calculations also reveal the following findings.

(1) Under the conditions of nominally uniaxial strain that involve high stress triaxiality, the α-quartz-to-coesite phase transformation decreases the load-carrying capacity of the material relative to the case without transformation, although this effect is relatively small.
(2) The phase transformation increases the total energy-dissipation capacity of materials by up to 18.5%, even though the transformation itself dissipates less than 2% of the total energy input into the material during a loading event. This disproportional influence is a result of the effect of the transformation on fracture. Specifically, the phase transformation can increase the energy dissipated through crack surface friction by 100% by enhancing the development of cracks. Higher porosity levels and higher fiber volume fractions can reduce this effect of phase transformation, with the effect of fibers being more pronounced.
(3) The phase transformation decreases the energy dissipated through inelastic deformation, and this influence diminishes as aggregate and porosity volume fraction increases.

It is useful to point out that the forgoing study does not account for the effect of temperature changes on the phase transformation of the quartz aggregate and the thermal softening of steel fibers. These thermal effects should be considered in future studies.

Acknowledgements

This research was sponsored by the US Department of Homeland Security, Science and Technology Directorate, Infrastructure Protection and Disaster Management Division: Ms. Mila Kennett, Program Manager. The research was performed under the direction of Dr. Beverly P. DiPaolo, Engineering Research and Development Center (ERDC), US Army Corps of Engineers. Permission to publish was granted by the Director, Geotechnical and Structures Laboratory, ERDC. Approved for public release; distribution is unlimited.

This research is part of a basic research demonstration project on improvised explosive device effects and is performed in collaboration with the ERDC – Geotechnical and Structures Laboratory (GSL), Oak Ridge National Laboratory, and Sandia National Laboratories.

Views expressed are solely those of the authors and do not necessarily reflect the opinions or policy of the US Department of Homeland Security, the US Army Corps of Engineers, or any other agency of the US Government, and no official endorsement should be inferred.

The authors would also like to thank Brett Ellis and Chris Lammi for their contributions to the development of the concrete structure instantiation code used in this study. MZ also acknowledges support from the National Research Foundation of Korea through WCU Grant No. R31-2009-000-10083-0 at Seoul National University where he is a World Class University (WCU) Professor.

References

Abaqus v6.10 Theory Manual. 2010, Dassault Systemes.

Abell, A.B., Lange, D.A., 1998. Fracture mechanics modeling using images of fractured surfaces. International Journal of Solids and Structures 35 (31–32), 4025–4033.

Aragao, F.T., Kim, Y., Lee, J., Allen, D., 2010. Micromechanical model for heterogeneous asphalt concrete mixtures subjected to fracture failure. Journal of Materials in Civil Engineering 23 (1), 30–38.

Benzeggagh, M.L., Kenane, M., 1996. Measurement of mixed-mode delamination fracture toughness of unidirectional glass/epoxy composites with mixed-mode bending apparatus. Composites Science and Technology 56 (4), 439–449.

Blacic, J.D., Christie, J.M., 1984. Plasticity and hydrolitic weakening of quartz single crystals. Journal of Geophysical Research 89 (B6), 4223–4239.

Boettger, J.C., Lyon, S.P., 1990. New multiphase equation of state for polycrystalline quartz. Los Alamos National Laboratory, Los Alamos, New Mexico.

Bose, K., Ganguly, J., 1995. Quartz coesite transition revisited. American Mineralogist 80, 231–238.

Buck, J.J., McDowell, D.L., Zhou, M., 2012. Effect of microstructure on load-carrying and energy-dissipation capacities of UHPC. Cement and Concrete Research 43 (2013), 34–50.

Building Code Requirements for Structural Concrete (ACI 318–95), 1995. American Concrete Institute, Farmington Hills, Michigan, p. 369.

Calderon, E., Gauthier, M., Decremps, F., Hamel, G., Syfosse, G., Polian, A., 2007. Complete determination of the elastic moduli of α-quartz under hydrostatic pressure up to 1 GPa: an ultrasonic study. Journal of Physics: Condensed Matter 19 (43), 1–13.

Camacho, G.T., Ortiz, M., 1996. Computational modelling of impact damage in brittle materials. International Journal of Solids and Structures 33 (20–22), 2899–2938.

Camanho, P.P., Davila, C.G., de Moura, M.F., 2003. Numerical simulation of mixed-mode progressive delamination in composite materials. Journal of Composite Materials 37 (16), 1415–1438.

Carpinteri, A., Valente, S., Ferrara, G., Melchiorri, G., 1993. Is mode II fracture energy a real material property? Computers & Structures 48 (3), 397–413.

Cavil, B., Rebentrost, M., Perry, V., 2006. Ductal – an ultra-high performance material for resistance to blast and impacts. In: First Specialty Conference on Disaster Mitigation, Calgary, Alberta, Canada.

Choi, H.-J., McDowell, D., Allen, J.K., Rosen, D., Mistree, F., 2008. An inductive design exploration method for robust multiscale materials design. Journal of Mechanical Design 130, 031402–031413.

Drucker, D.C., Prager, W., 1952. Soil mechanics and plastic analysis or limit design. Quarterly of Applied Mathematics 10, 157–165.

Ellis, B.D., Zhou, M., McDowell, D.L., 2012. Energy dissipation and strength evolution of Ultra-High-Performance Fiber-Reinforced Concrete (UHPFRC), in Proceedings of HiPerMat 2012 Third International Symposium on UHPC and Nanotechnology for High Performance Construction Materials, Kassel University Press, Kassel, Germany, 2, 273-281.

Flynn, D.R., 1998. Response of High Performance Concrete to Fire Conditions: Review of Thermal Property Data and Measurement Techniques. National Institute of Standards and Technology, Building and Fire Research Laboratory.

Fracture Mechanics of Concrete Structures, 1992. In: International Conference on Fracture Mechanics of Concrete Structures. Beaver Run Resort, Breckenridge, CO, CRC Press.

Gens, A., Carol, I., Alonso, E.E., 1989. An interface element formulation for the analysis of soil-reinforcement interaction. Computers and Geotechnics 7 (1–2), 133–151.

Handoo, S.K., Agarwal, S., Agarwal, S.K., 2002. Physiochemical, mineralogical, and morphological characteristics of concrete exposed to elevated temperatures. Cement and Concrete Research 32 (7), 1009–1018.

Hill, R., 1952. The elastic behavior of a crystalline aggregate. Proceedings of the Physical Society, Section A 65 (5), 349–354.

Hillerborg, A., Modeer, M., Petersson, P.E., 1976. Analysis of crack formation and crack growth in concrete by means of fracture mechanics and finite elements. Cement Concrete Research 6, 773–782.

Kimizuka, H., Ogata, S., Li, J., 2008. Hydrostatic compression and high-pressure elastic constants of coesite silica. AIP 103, 053506.

Lammi, C., Li, H., McDowell, D., Zhou, M., Dynamic fracture and dissipation behaviors of concrete at the mesoscale. Cement and Concrete Composites, submitted for publication.

Lammi, C., McDowell, D., Zhou, M., 2011. Prediction of damage initiation in ultra high-performance concrete during rapid heating. In: US National Congress on Computational Mechanics, Minneapolis, MN.

Li, V., 1994. Determination of interfacial debond mode for fiber-reinforced cementitious composites. Journal of Engineering Mechanics 120 (4), 707–720.

Morsy, M.S., Alsayed, S.H., Aqel, M., 2010. Effect of elevated temperature on mechanical properties and microstructure of silica flour concrete. International Journal of Civil & Environmental Engineering 10 (1), 1–6.

Mosler, J., Schneider, I., 2011. A thermodynamically and variationally consistent class of damage-type coheisve models. Journal of the Mechanics and Physics of Solids 59, 1647–1668.

Naus, D.J., 2010. A compilation of elevated temperature concrete material property data and information for use in assessments of nuclear power plant reinforced concrete structures. Oak Ridge National Laboratory.

Omer, A., 2007. Effects of elevated temperatures on properties of concrete. Fire Safety Journal 42 (8), 516–522.

Park, K., Paulino, G., Roesler, J., 2009. A unified potential-based cohesive model of mixed-mode fracture. Journal of the Mechanics and Physics of Solids 57, 891–908.

Petersson, P.E., 1981. Crack growth and development of fracture zone in plane concrete and similar materials. Lund Institute of Technology, Lund, Sweden.

Roesler, J., Paulino, G.H., Park, K., Gaedicke, C., 2007. Concrete fracture prediction using bilinear softening. Cement and Concrete Composites 29 (4), 300–312.

Rong, Z., Sun, W., Zhang, Y., 2010. Dynamic compression behavior of ultra-high performance cement based composites. International Journal of Impact Engineering 37 (5), 515–520.

Shen, B., Paulino, G.H., 2011. Identification of cohesive zone model and elastic parameters of fiber-reinforced cementitious composites using digital image correlation and a hybrid inverse technique. Cement and Concrete Composites 33 (5), 572–585.

Swamy, R.N., Mangat, P.S., 1974. A theory for the flexural strength of steel fiber reinforced concrete. Cement and Concrete Research 4 (2), 313–325.

Tomar, V., Zhai, J., Zhou, M., 2004. Bounds for element size in a variable stiffness cohesive finite element model. International Journal for Numerical Methods in Engineering 61, 1894–1920.

Wang, J.-A.J., Mattus, C.H., Ren, F., 2010. DHS counter improvised explosive device effects basic research. Geotechnical and Structures Laboratory, Engineering Research and Development Center, US Army Corps of Engineers.

Xu, X.-P., Needleman, A., 1993. Void nucleation by inclusion debonding in a crystal matrix. Modelling and Simulation in Materials Science and Engineering 1 (2), 111–132.

Zhai, J., Tomar, V., Zhou, M., 2004. Micromechanical simulation of dynamic fracture using the cohesive finite element method. Journal of Engineering Materials and Technology 126, 179–191.

Zhou, Y., 2005. An experiment study of quartz-coesite transition at differential stress. Chinese Science Bulletin 50 (5), 445–451.

Zhou, X.Q., Kuznetsov, V.A., Hao, H., Waschl, J., 2008. Numerical prediction of concrete slab response to blast loading. International Journal of Impact Engineering 35 (10), 1186–1200.